J. Fluid Mech. (2013), *vol.* 715, *pp.* 134–162. © Cambridge University Press 2013
doi:10.1017/jfm.2012.503

Clustering and turbulence modulation in particle-laden shear flows

P. Gualtieri[1,†], F. Picano[2], G. Sardina[3,2] and C. M. Casciola[1]

[1]Dipartimento di Ingegneria Meccanica e Aerospaziale, Università di Roma *La Sapienza* Via Eudossiana 18, 00184 Roma, Italy

[2]Linné Flow Center, KTH Mechanics, Osquars Backe 18, SE-100 44 Stockholm, Sweden

[3]UKE - Università Kore di ENNA Facoltà di Ingegneria, Architettura e Scienze Motorie, Via delle Olimpiadi, 94100 Enna, Italy

(Received 14 April 2012; revised 13 July 2012; accepted 9 October 2012)

Turbulent fluctuations induce the common phenomenon known as clustering in the spatial arrangement of small inertial particles transported by the fluid. Particles spread non-uniformly, and form clusters where their local concentration is much higher than in nearby rarefaction regions. The underlying physics has been exhaustively analysed in the so-called one-way coupling regime, i.e. negligible back-reaction of the particles on the fluid, where the mean flow anisotropy induces preferential orientation of the clusters. Turbulent transport in suspensions with significant mass in the disperse phase, i.e. particles back-reacting in the carrier phase (the two-way coupling regime), has instead been much less investigated and is still poorly understood. The issue is discussed here by addressing direct numerical simulations of particle-laden homogeneous shear flows in the two-way coupling regime. Consistent with previous findings, we observe an overall depletion of the turbulent fluctuations for particles with response time of the order of the Kolmogorov time scale. The depletion occurs in the energy-containing range, while augmentation is observed in the small-scale range down to the dissipative scales. Increasing the mass load results in substantial broadening of the energy cospectrum, thereby extending the range of scales driven by anisotropic production mechanisms. As discussed throughout the paper, this is due to the clusters which form the spatial support of the back-reaction field and give rise to a highly anisotropic forcing, active down to the smallest scales. A certain impact on two-phase flow turbulence modelling is expected from the above conclusions, since the frequently assumed small-scale isotropy is poorly recovered when the coupling between the phases becomes significant.

Key words: homogeneous turbulence, multiphase and particle-laden flows, turbulent flows

1. Introduction

Transport of inertial particles is involved in several fields of science such as droplet growth and collisions in clouds (Falkovich, Fouxon & Stepanov 2002; Wang *et al.* 2008), plankton accumulation in the oceans (Lewis & Pedley 2000; Károlyi *et al.* 2002), or plume formation in the atmosphere (Woods 2010). At the same time,

† Email address for correspondence: p.gualtieri@caspur.it

https://doi.org/10.1017/jfm.2012.503 Published online by Cambridge University Press

multiphase flow is the basis of several technological applications. The dynamics of inertial particles is crucial to the design of injection systems of internal combustion engines (Post & Abraham 2002), prevention of sediment accumulation in pipelines (Rouson & Eaton 2001; Portela, Cota & Oliemans 2002), and for the appropriate sizing of several industrial devices: see Derksen, Sundaresan & Van Der Akker (2006) and the review by Van der Hoef *et al.* (2008).

The relevant physical aspect of particle dynamics consists in their finite inertia, which prevents them from following the fluid trajectories. Consequently, interesting features emerge. Most evident is the 'preferential accumulation' which, in inhomogeneous flows such as wall-bounded flows, occurs in the form of the so-called 'turbophoresis', i.e. preferential localization of particles in the near-wall region (Reeks 1983; Brooke *et al.* 1992). An exhaustive review of the subject can be found in Soldati & Marchioli (2009); see also Marchioli & Soldati (2002) and Picano, Sardina & Casciola (2009) for a physical explanation in terms of the statistical properties of velocity fluctuations in the near-wall region. When the idealized conditions of isotropic turbulence are addressed, preferential accumulation manifests itself in the form of small-scale clustering. The disperse phase forms small-scale clusters where most particles concentrate, separated by void regions of small particle density. This issue is now well understood and documented, as shown by the large literature available on the subject: see e.g. Eaton & Fessler (1994), Reade & Collins (2000), Bec *et al.* (2007) and Yoshimoto & Goto (2007).

So far the effect of turbulent transport on particle dynamics has been studied extensively in many flow configurations. Much less is known about the effect the disperse phase may have on the carrier flow, demanding renewed effort in this direction: see e.g. the recent reviews by Eaton (2009) and Balachandar & Eaton (2010). It is expected that, under proper coupling conditions, the momentum exchange between the two phases might become relevant in driving the turbulent fluctuations away from their universal equilibrium state, predicted by Kolmogorov in the early 1940s (Kolmogorov 1941). In contrast to the one-way coupling regime, addressing these effects calls into play the more realistic two-way coupling mechanism, where the disperse phase provides an active modulation of velocity fluctuations.

In this context, many authors first studied the simplest flow configuration, i.e. homogeneous isotropic turbulence. The first simulations go back to the 1990s. For instance Squires & Eaton (1990) analysed the modification of statistically steady isotropic turbulence. They found an overall attenuation of the turbulent kinetic energy and the energy dissipation rate induced by the particles. At the same time the energy spectra showed a broad attenuation in the energy-containing range and substantial augmentation in the high wavenumber range, indicating non-uniform distortion of turbulence due to two-way coupling effects; see also Boivin, Simonin & Squires (1998). Elghobashi & Truesdell (1993) addressed decaying isotropic turbulence, showing that both the decay rate of turbulent kinetic energy and the viscous dissipation rate occurring in the fluid phase were enhanced in the two-way coupling regime. The authors confirmed the selective spectral redistribution of energy rather than a uniform augmentation or attenuation. They also addressed the effect of gravity, showing that the alteration of turbulence occurred in an anisotropic manner. Similar results were found by Sundaram & Collins (1999), who performed a systematic analysis by changing both the response time of the particles and the mass loading ratio. Further studies by Druzhinin & Elghobashi (1999) and Druzhinin (2001) reconsidered the alteration of decaying isotropic turbulence, showing that the modification of turbulent kinetic energy and energy dissipation rate was controlled by the particle response

https://doi.org/10.1017/jfm.2012.503 Published online by Cambridge University Press

time τ_p. Particles with response time much smaller than the Kolmogorov time scale τ_η led to an augmentation of both turbulent kinetic energy and dissipation rate, while particles with response time of the order of or larger than the Kolmogorov time scale led to a depletion of both. This behaviour was explained in terms of the spectral distribution of the momentum coupling term. Ferrante & Elghobashi (2003) addressed the energy spectra. For particle response time smaller than the Kolmogorov time scale ($\tau_p < \tau_\eta$) they found enhancement of the spectra at all wavenumbers, while for $\tau_p > \tau_\eta$ they observed depletion at all scales. Interestingly, cases with $\tau_p \sim \tau_\eta$ showed a pivoting effect in the spectra with large-scale attenuation and small-scale augmentation. The main parameters controlling the augmentation/attenuation of turbulent fluctuations in statistically homogeneous conditions are the mass loading of the disperse phase and the Stokes number $St_\eta = \tau_p/\tau_\eta$. These are the only dimensionless numbers controlling the dynamics of the disperse phase for particle diameters sufficiently smaller than the viscous (Kolmogorov) scale of the flow, at least when the particle Reynolds number is small enough to allow neglect of wake effects and the suspension is sufficiently diluted that the average inter-particle distance is much larger than the particle size. However, it is worth stressing that when finite-size particles are considered alternative parameters are needed: see Lucci, Ferrante & Elghobashi (2011). Finite-size effects become relevant for particles with diameter larger than the Kolmogorov scales. In this case Yeo *et al.* (2010) showed the existence of a cross-over wavenumber between dumped and enhanced energy modes, which was found to scale with the particle diameter. Recently Gao, Li & Wang (2011) re-addressed the issue and concluded that, although the cross-over wavenumber is indeed controlled by the particle diameter, the density ratio constitutes a second independent parameter.

Concerning experiments, several studied statistically steady isotropic flows in confined vessels. Hwang & Eaton (2006*a*) reported the attenuation of both the turbulent kinetic energy and the viscous dissipation rate at $\tau_p > \tau_\eta$. The same trend was confirmed under micro-gravity conditions (Hwang & Eaton 2006*b*). The adoption of particle image velocimetry with sub-Kolmogorov resolution allowed Tanaka & Eaton (2010) to document the augmentation of the energy dissipation rate near the particle boundaries.

In general, papers concerning particle-laden flows form a large body of literature. Important issues such as the increase of the particles' settling velocity have been addressed both numerically (Bosse, Kleiser & Meiburg 2006) and experimentally (Yang & Shy 2005). By breaking isotropy, gravity forces the preferential intensification of turbulence in the vertical direction with augmentation in the transverse directions observed only below the Taylor scale. Momentum coupling effects between the two phases have also been observed in the context of grid-generated spatially decaying turbulence: see e.g. Geiss *et al.* (2004) and Poelma, Westerweel & Ooms (2007) and the extensive review of back-reaction effects on isotropic turbulence by Poelma & Ooms (2006).

Concerning wall-bounded flows, relatively few authors have considered the classical geometry of the pipe (see e.g. Ljus, Johansson & Almsedt (2002) and Rani, Winkler & Vanka (2004)), with most investigations devoted to channel flows. The work by Kulick, Fessler & Eaton (1994) on channel flow documented a progressive attenuation of turbulence fluctuations for increasing particle inertia, mass load and distance from the wall. The authors found a preferential attenuation of the cross-flow velocity fluctuations. Later on Paris & Eaton (2001) reported an attenuation of the energy dissipation rate and of the Reynolds shear stress. The particle Reynolds number was

https://doi.org/10.1017/jfm.2012.503 Published online by Cambridge University Press

identified to be an important parameter for turbulence attenuation. Pan & Banerjee (2001) conducted a direct numerical simulation of a turbulent channel flow seeded with small particles, focusing on the effect of the particle diameter on the reduction of turbulent fluctuations. More recently Tanaka & Eaton (2008), by reviewing the available data for wall-bounded flows, introduced a suitable dimensionless parameter – the particle momentum number – which was able to identify ranges where attenuation/augmentation of turbulent kinetic energy occurs; see also the review by Gore & Crowe (1989) and by Hetsroni (1989). The preferential distortion of turbulence due to two-way coupling effects has been addressed by Li *et al.* (2001), while Zhao, Andersson & Gillisen (2010) demonstrated how micro-particles might lead to an overall drag reduction presumably associated with a substantial modification of the coherent quasi-streamwise vortices; see also Bijlard *et al.* (2010).

In this paper we address the modification of turbulence by relating the preferential alteration of velocity fluctuations to the anisotropy of the clusters. In fact, as isotropy is broken, e.g. by gravity or mean shear, the back-reaction of the disperse phase generates strong anisotropy in the carrier phase. For instance, Ahmed & Elghobashi (2000) reported a substantial reduction of turbulent kinetic energy associated with an increase of the energy dissipation rate in the context of a time-evolving homogeneous shear flow. The same authors showed that the large-scale anisotropy of the flow was augmented by the back-reaction of the particles, as also reported by Mashayek (1998). Motivated by recent findings in the context of anisotropic clustering (Shotorban & Balachandar 2006; Gualtieri, Picano & Casciola 2009), we consider here the modulation of turbulence, addressing the particle-laden homogeneous shear flow in the two-way coupling regime. Such flow can be considered as a sort of bridge between the idealized conditions of isotropic turbulence and the more realistic geometries of wall-bounded flows, since it preserves spatial homogeneity and retains the anisotropy typical of wall-bounded flows. Under shear, turbulent fluctuations are strongly anisotropic at the largest scales due to production of turbulent kinetic energy via interaction of the mean velocity gradient and turbulent fluctuations. At smaller scales, below the so-called shear scale $L_S = \sqrt{\epsilon/S^3}$ – where ϵ is the mean dissipation rate and S the mean shear – inertial energy transfer usually prevails; see e.g. Jacob *et al.* (2008) for a discussion of high-accuracy wind tunnel data. In these conditions re-isotropization of turbulent fluctuation takes place following a route described in Casciola *et al.* (2005, 2007). In such flow, turbulent fluctuations in the one-way coupling regime are found to induce the anisotropic clustering of the disperse phase which persists down to the smallest scales (Gualtieri *et al.* 2009). In contrast to the behaviour of velocity fluctuations, particle configurations do not lose their directionality at small scales. Their anisotropy increases down to the viscous scales, where clusters still keep a memory of the spatial orientation induced by the large-scale motions, leading to a substantial departure from isotropy of the inter-particle collision rate: see Gualtieri *et al.* (2012).

Here we consider the same flow in the two-way coupling scenario. We will show that in these more complex conditions the small-scale anisotropic clusters act as sources/sinks of momentum for the fluid turbulent motions distributed all along the range of scale, operating a sort of fractal forcing of the carrier flow (Stresing *et al.* 2010). They deplete the energy from the largest inertial scales, which is in part retrieved in the low-inertial/dissipative range, where the clusters keep the velocity fluctuations to a higher excitation state than expected on the basis of the standard Kolmogorov theory. The effect is found to be highly anisotropic in shear flow, and

https://doi.org/10.1017/jfm.2012.503 Published online by Cambridge University Press

prevents the small-scale fluid motions from recovering isotropy, which eventually increases due to the momentum exchange with the disperse phase.

The paper is organized as follows. In § 2 we address the numerical methodology for the simulation of the two-way coupled particle-laden homogeneous shear flow, and we present the dataset. In § 3 we describe particle clustering under the two-way coupling regime, while § 4 concerns turbulence modification. A final discussion is given in § 5.

2. Methodology

In this section we address the model of the particle-laden turbulent flow and the relevant numerical techniques. The carrier flow is a statistically steady homogeneous shear flow with the disperse phase consisting of diluted point-like inertial particles.

Modelling the back-reaction in numerical simulations is an issue: see e.g. the recent review by Wang *et al.* (2009), where an exhaustive discussion concerning the available methodologies is given. The local distortion of turbulence due to the disperse phase can be fully captured only by resolving the boundary of each particle – resolved particle simulations – with several possible approaches. Burton & Eaton (2005) use a finite volume method where no-slip boundary conditions are directly enforced at the particle boundary. Alternatively (see e.g. the recent study by Lucci, Ferrante & Elghobashi 2010), a suitable surface force is imposed on each particle boundary in the immersed boundary method to enforce the no-slip conditions of the surrounding fluid. The lattice Boltzmann method (Cate *et al.* 2004; Poesio *et al.* 2006) has also been used for two-way coupling simulations, exploiting its ability to deal with complex boundaries.

Other approaches approximate the flow close to small particles as a Stokes flow. Zhang & Prosperetti (2005) used the Stokes solution to provide appropriate boundary conditions for the Navier–Stokes equations close to each particle. In the force coupling method (Lomholt & Maxey 2003), the disturbance flow produced by the particles is modelled as a regularized steady Stokes solution corresponding to a force monopole, while the singular steady Stokes solution is employed by Pan & Banerjee (2001).

The approaches discussed above are feasible only for a relatively small number of large particles, i.e. particles whose diameter d_p is comparable to or larger than the Kolmogorov scale η. Indeed, such methods are computationally too expensive to deal with millions of sub-Kolmogorov particles injected into the flow. In the limit $d_p \ll \eta$, the disperse phase can be considered as consisting of point particles, i.e. as point sources/sinks of momentum for the carrier fluid. In this limit millions of particles can be efficiently handled, at the price of losing the finest detail of the interaction between the two phases. In this context the particle-in-cell method introduced by Crowe, Sharma & Stock (1977) is still a valuable approach to modelling the two-way coupling regime, even though it must be handled with care to avoid lack of numerical convergence in the interphase momentum transfer (Garg, Narayanan & Subramaniam 2009).

2.1. *Fluid phase*

Concerning the carrier fluid, the velocity field $\boldsymbol{v}$ is decomposed into a mean flow $\boldsymbol{U} = Sx_2\,\boldsymbol{e}_1$ and a fluctuation $\boldsymbol{u}$, where $\boldsymbol{e}_1$ is the unit vector in the streamwise direction, x_2 denotes the coordinate in the direction of the mean shear S (transverse direction) and x_3 points in the spanwise direction. Rogallo's technique (Rogallo 1981) is employed to rewrite the Navier–Stokes equations for velocity fluctuations in a deforming coordinate system convected by the mean flow according to the

https://doi.org/10.1017/jfm.2012.503 Published online by Cambridge University Press

transformation of variables $\xi_1 = x_1 - Stx_2$; $\xi_2 = x_2$; $\xi_3 = x_3$; $\tau = t$. The resulting system,

$$\boldsymbol{\nabla} \cdot \boldsymbol{u} = 0, \quad \frac{\partial \boldsymbol{u}}{\partial \tau} = (\boldsymbol{u} \times \boldsymbol{\zeta}) - \boldsymbol{\nabla}\pi + \nu \nabla^2 \boldsymbol{u} - Su_2 \boldsymbol{e}_1 + \boldsymbol{F}, \tag{2.1}$$

is numerically integrated by a pseudospectral method combined with a fourth-order Runge–Kutta scheme for temporal evolution. In (2.1) $\boldsymbol{\zeta}$ is the curl of $\boldsymbol{u}$, π is the modified pressure which includes the fluctuating kinetic energy $|\boldsymbol{u}|^2/2$, ν is the kinematic viscosity and $\boldsymbol{F}$ denotes the body force associated with the back-reaction of the disperse phase, which we will address in detail in the following subsections. Note that $\boldsymbol{\xi} = (\xi_1, \xi_2, \xi_3)$ is used consistently throughout the paper to denote a point in computational space. The Navier–Stokes equations are integrated in a $4\pi \times 2\pi \times 2\pi$ periodic box on a computational grid of $N_x \times N_y \times N_z$ Fourier modes corresponding to N_c cells. The nonlinear term is computed in physical space, where the standard 3/2 rule is adopted to remove aliasing errors. Due to the transformation of variables, the computational grid is distorted by the mean flow advection in physical space. To allow long time integrations the computational grid is re-meshed into a non-skewed grid at every re-mesh period $T_R = 2/S$, exploiting the periodicity in the streamwise direction: see Gualtieri *et al.* (2002) for further details on the numerics. The possibility of reaching statistical stationarity for the homogeneous turbulent shear in a confined box was first demonstrated by Pumir & Shraiman (1994) and Pumir (1996). In such conditions, the flow presents a pseudo-cyclic behaviour with recurrent fluctuations in the turbulent kinetic energy and the enstrophy. Turbulent fluctuations are stationary in the sense that the pseudo-cyclic oscillations repeat themselves indefinitely and yield ensemble averages which are time-independent: see e.g. the discussion in Gualtieri *et al.* (2007), where most of the literature on the subject available at that time was reported.

2.2. *Disperse phase*

The disperse phase consists of N_p diluted particles, with an average of N_p/N_c particles per cell, having mass density ρ_p much larger than the carrier fluid ρ_f and diameter d_p much smaller than the smallest turbulent scales, i.e. the Kolmogorov dissipative scale η. In these conditions, among the different forces known to act on a particle (see Maxey & Riley 1983 for a complete analysis), the only relevant contribution arises from the Stokes drag. The equations for particle position $x_i^p(t)$ and velocity $v_i^p(t)$ then read

$$\frac{\mathrm{d}x_i^p}{\mathrm{d}t} = v_i^p, \quad \frac{\mathrm{d}v_i^p}{\mathrm{d}t} = \frac{1}{\tau_p}[v_i(x_1^p, x_2^p, x_3^p, t) - v_i^p(t)], \tag{2.2}$$

where $v_i(x^p, t)$ is the instantaneous fluid velocity evaluated at $x_i^p(t)$ and $\tau_p = \rho_p d_p^2/(18\nu\rho_f)$ is the Stokes relaxation time. When dealing with the homogeneous shear flow, it is instrumental to decompose the particle velocity as $v_i^p = U_i[x_k^p(t)] + u_i^p$, where u_i^p denotes the particle velocity deviation with respect to the local mean flow of the carrier fluid. By using Rogallo's transformation equations (2.2) can be written in computational space as

$$\frac{\mathrm{d}\xi_i^p}{\mathrm{d}\tau} = u_i^p - S\tau u_2^p \delta_{i1}, \quad \frac{\mathrm{d}u_i^p}{\mathrm{d}\tau} = f_i^p, \tag{2.3}$$

where $f_i^p = \tau_p^{-1}\left[u_i(\xi_1^p, \xi_2^p, \xi_3^p, \tau) - u_i^p(\tau)\right] - Su_2^p\delta_{i1}$ is the expression of the Stokes drag acting on the pth particle. Equations (2.3) are integrated by the same fourth-order

https://doi.org/10.1017/jfm.2012.503 Published online by Cambridge University Press

Runge–Kutta scheme as used for the Navier–Stokes equations, and the interpolation of the fluid velocity at the particle positions adopts a trilinear scheme.

2.3. *Modelling of two-way coupling*

In the two-way coupling regime the particle volume fraction is still small enough to neglect particle–particle collisions and hydrodynamic interactions. However the mass loading on the fluid is large due to the high particle–fluid density ratio, which makes the momentum exchange between the two phases significant: see e.g. Elgobashi (2006). In the context of the point particle method two issues require some care: the evaluation of the Stokes drag on the particles and the computation of the back-reaction force $\boldsymbol{F}$ on the carrier phase.

The notion of Stokes drag pertains to the force exerted by a uniform stream $\boldsymbol{U}_\infty$ of fluid impinging on a single particle, $\boldsymbol{f}^p \propto \boldsymbol{U}_\infty - \boldsymbol{v}^p$. The expression can be interpreted in terms of slip velocity, as the undisturbed (i.e. in the absence of the particle) relative fluid–particle velocity at the particle position. In the one-way coupling regime, for particles much smaller than the relevant spatial scale of the incoming flow, the Kolmogorov scale in the present case, the concept is naturally extended by considering the local fluid velocity, i.e. the fluid velocity at the particle position. However, in the two-way coupling regime difficulties arise due to the particle disturbance on the surrounding fluid, since the slip velocity on the pth particle should retain the contributions from the background flow and from all the other $N_p - 1$ particles except for the self-interaction of the pth particle with itself. In fact, avoiding this self-interaction, though possible in principle, is indeed unaffordable. The most effective algorithms (e.g. the particle-in-cell method) achieve the result by relying on the statistical nature of the force due to a large number of particles, combined with suitable interpolations of the back-reaction force and fluid velocity. In the algorithm, the back-reaction of a single particle on the fluid is redistributed by reverse interpolation on the grid nodes, where the contributions of all the particles belonging to the cell are added. When the fluid velocity is advanced in time on the discrete grid, the resulting flow is affected by the back-reaction of all the N_p/N_c particles in the cell, with all the contributions having the same order of magnitude. It follows that the slip velocity interpolated at the position of the pth particle retains the spurious self-term, which gives rise to an error on the estimated slip velocity order of $1/(N_p/N_c)$: see e.g. Boivin *et al.* (1998), from which the present discussion draws abundantly. In principle, the spurious self-interaction could be removed assuming that the self-disturbance flow is described by a steady Stokeslet. The Stokeslet can also be used to estimate the error arising from retaining the self-interaction, considering that the average particle-grid node distance is of the order of the grid size Δ, leading to the error scaling as d_p/Δ (Boivin *et al.* 1998). The present discussion shows that convergence of the particle-in-cell method for two-way coupling simulations needs to be carefully validated upon refinement of both grid size and number of particles per cell, with the ratio $d_p/\Delta \ll 1$ playing a significant role for physical consistency.

Concerning the second issue, i.e. the evaluation of the back-reaction $\boldsymbol{F}$ on the carrier phase, the influence of the pth particle on the fluid is accounted for by a Dirac delta function centred at the particle position

$$\boldsymbol{F}\left(\boldsymbol{\xi}, \boldsymbol{\xi}^p\right) = -\frac{m_p}{\rho_f} \boldsymbol{f}^p \left[\boldsymbol{\xi}^p(\tau), \tau\right] \delta \left[\boldsymbol{\xi} - \boldsymbol{\xi}^p(\tau)\right]. \tag{2.4}$$

In the spirit of the particle-in-cell method, the force on the fluid is regularized by averaging the singular field given by (2.4) on the computational cell of volume ΔV_{cell}

https://doi.org/10.1017/jfm.2012.503 Published online by Cambridge University Press

the particle belongs to, namely

$$\bar{\boldsymbol{F}}\left(\boldsymbol{\xi}^p\right) = -\frac{1}{\Delta V_{cell}}\frac{m_p}{\rho_f}\boldsymbol{f}^p\left[\boldsymbol{\xi}^p(\tau),\tau\right]. \tag{2.5}$$

The back-reaction given by (2.5) is still known at the particle position $\boldsymbol{\xi}^p$ in computational space which, in general, does not coincide with the grid nodes where the fluid velocity is updated. Hence the force $\bar{\boldsymbol{F}}(\boldsymbol{\xi}^p)$ must be redistributed among the eight vertices $\boldsymbol{\xi}^c_q, q = 1,\ldots,8$ of the cth cell where the particle is located. The forces at the vertices $\bar{\boldsymbol{F}}(\boldsymbol{\xi}^c_q)$ are determined by requiring that the resulting force and torque with respect to the pole $\boldsymbol{\xi}^p$ are conserved, i.e. $\sum_q \bar{\boldsymbol{F}}(\boldsymbol{\xi}^c_q) = \bar{\boldsymbol{F}}(\boldsymbol{\xi}^p)$, $\sum_q(\boldsymbol{\xi}^c_q - \boldsymbol{\xi}^p)\times\bar{\boldsymbol{F}}(\boldsymbol{\xi}^c_q) = 0$. This procedure is repeated for all the particles in the cell, allowing for a proper momentum and torque coupling between the two phases. The procedure can be shown to be consistent with the balance of the total energy of the system (fluid and particles): see e.g. Sundaram & Collins (1996). The approach works properly whenever the number of particles per cell is sufficiently large and the grid size accurately resolves the Kolmogorov scale, $\Delta \ll \eta$, to ensure that the particles affect the carrier flow at the smallest scales, i.e. $d_p \ll \Delta \ll \eta$ and $N_p/N_c \gg 1$.

2.4. *Dataset*

The data we analyse pertain to a statistically steady direct numerical simulation (DNS) of a homogeneous shear flow. The mean shear induces velocity fluctuations which are strongly anisotropic at the larger scales driven by production, while at smaller separations the classical energy transfer mechanisms become effective in inducing re-isotropization. Based on this knowledge, the position of the shear scale L_S was found to be crucial in determining whether small-scale isotropy recovery eventually occurs. For these reasons L_S plays an important physical role in shear turbulence, where it enters into the two basic control parameters (Gualtieri *et al.* 2002; Shumacher 2004). The first one is the Corrsin parameter, $S^*_c = S\,(\nu/\epsilon)^{1/2} = (\eta/L_S)^{2/3}$, where η is the Kolmogorov scale. The Corrsin parameter can be recast in terms of the Taylor–Reynolds number $1/S^*_c \propto Re_\lambda = \sqrt{5/(\nu\epsilon)}\langle u_\alpha u_\alpha\rangle$, where ν is the kinematic viscosity, u_α is the αth Cartesian component of the velocity fluctuation, and the angular brackets denote ensemble averaging. The second parameter is the shear strength $S^* = S\langle u_\alpha u_\alpha\rangle/\epsilon = (L_0/L_S)^{2/3}$, with L_0 the integral scale of the flow. The Corrsin parameter determines the extension of the range of scales below the shear scale and above the Kolmogorov length η. When this range is sufficiently extended, i.e. the Taylor–Reynolds number is large enough, small-scale isotropy recovery is likely to occur in the fluid velocity field. The shear strength, instead, fixes the range of scales directly affected by the geometry of the forcing. This is the anisotropic range between integral and shear scale.

Concerning the disperse phase, the dynamics is controlled by the ratio of the particle relaxation time τ_p to a characteristic flow time scale, typically the Kolmogorov time scale $\tau_\eta = (\nu/\epsilon)^{1/2}$, i.e. the relevant control parameter is the Stokes number $St_\eta = \tau_p/\tau_\eta$. When the two-way coupling regime is considered, other non-dimensional parameters are required to describe the momentum exchange between the two phases, namely the mass load fraction $\Phi = M_p/M_f$, defined as the ratio between the mass of the disperse phase $M_p = \rho_p V_p$ and the carrier fluid $M_f = \rho_f V_f$. The mass fraction may be expressed as $\Phi = (\rho_p/\rho_f)\Phi_V$, where the density ratio ρ_p/ρ_f is assumed to be much larger than unity to achieve appreciable loads even in dilute suspensions where the volume

https://doi.org/10.1017/jfm.2012.503 Published online by Cambridge University Press

fraction $\Phi_V = V_p/V_f$ is small. In the definition of the volume fraction $V_p = N_p \pi \rho_p d_p^3/6$ is the volume occupied by the N_p particles and V_f is the volume of the fluid.

In conclusion, the dimensionless quantities $\{S^*, Re_\lambda, St_\eta, \Phi\}$ are the four physical parameters that control the dynamics of two-way coupled particle-laden homogeneous shear flow in the asymptotic conditions $d_p \ll \eta$, $\rho_p \gg \rho_f$ and $\Phi_V \ll 1$. However, when dealing with numerical applications, other non-dimensional parameters must be considered, i.e. η/Δ, the ratio of Kolmogorov scale to grid size, and N_p/N_c, the ratio between the number of particles and cells. Convergence is achieved when the computed solution becomes independent from the two numerical parameters, being controlled only by the physical dimensionless ratios.

For the simulations summarized in table 1, the particles are injected into an already fully developed turbulent flow. They are initialized at random homogeneous positions with velocity matching the local fluid velocity. The dataset is organized into four sections labelled a, b, c, d, corresponding to different mass loads: $\Phi = 0, 0.2, 0.4, 0.8$. For each mass load the mean number of particles per cell and the grid resolution are systematically changed to assess the sensitivity to the numerical parameters and exclude numerical bias. In fact, to achieve the desired mass load Φ with a different number of particles per cell N_p/N_c and grid resolutions, the density ratio must be changed accordingly, i.e. increased with the square of the particle number. Density ratios as large as 10^6, though unrealistic, are nevertheless mandatory to understand convergence issues.

The statistical sample consists of 150 uncorrelated snapshots for the simulations performed on the finest grids, and order 450 and 900 snapshots for the intermediate and coarsest grids, respectively. After discarding the initial transient, snapshots are stored every re-meshing time $ST_r = 2$. In our simulation the large-scale correlation time of the flow, i.e. the integral time scale $\tau_0 = L_0/u_{rms}$, is $S\tau_0 = 1.5$, where $L_0 = u_{rms}^3/\epsilon$ is the integral scale, $u_{rms} = (2k/3)^{1/2}$, and $k = 0.5\rho_f \langle u_i u_i \rangle$ the turbulent kinetic energy.

3. Particle clustering

A visual impression of an instantaneous particle configuration is provided in figure 1, where slices of the domain in selected coordinate planes are shown for different values of the mass load parameter Φ at $St_\eta = 1.05$, where the Stokes number is defined with respect to the corresponding simulation in the one-way coupling regime.

In all the four cases shown in figure 1, the disperse phase shows accumulation regions and voids. The shear-induced orientation of the clusters is evident from the figure. A systematic description of anisotropic clustering under the two-way coupling conditions is achieved by considering the angular distribution functions (ADFs): see Gualtieri *et al.* (2009) for details. Essentially the ADF measures the number of particle pairs at separation r in the direction $\hat{\boldsymbol{r}}$, and is defined by

$$g(r, \hat{\boldsymbol{r}}) = \frac{1}{r^2} \frac{\mathrm{d}\nu_r}{\mathrm{d}r} \frac{1}{n_0}, \tag{3.1}$$

where $n_0 = 0.5 N_p (N_p - 1)/V_f$ is the volume density of particle pairs, and $\nu_r(r, \hat{\boldsymbol{r}})\,\mathrm{d}\Omega$ is the number of particle pairs contained in the spherical cone of radius r with axis along the direction $\hat{\boldsymbol{r}}$ and amplitude $\mathrm{d}\Omega$. The spherical average of the ADF, i.e. $g_{00}(r) = 1/(4\pi) \int_\Omega g(r, \hat{\boldsymbol{r}})\,\mathrm{d}\Omega$, is called the radial distribution function (RDF) and has already been used to characterize clustering in isotropic conditions: see e.g Sundaram &

https://doi.org/10.1017/jfm.2012.503 Published online by Cambridge University Press

https://doi.org/10.1017/jfm.2012.503 Published online by Cambridge University Press

Run	N_x	Φ	N_p/N_c	d_p/η	ρ_p/ρ_f	ϵ	k	Run	N_x	Φ	N_p/N_c	d_p/η	ρ_p/ρ_f	ϵ	k
a	192	0	—	—	—	0.088	0.556	b^7_{96}	96	0.2	7.4	0.018	5.4×10^4	0.068	0.513
$\hat{a}$	256	0	—	—	—	0.066	0.452	b^1_{96}	96	0.2	1	0.136	9.9×10^2	0.071	0.507
—	—	—	—	—	—	—	—	b^7_{192}	192	0.2	7.4	0.002	3.4×10^6	0.071	0.510
—	—	—	—	—	—	—	—	b^1_{192}	192	0.2	1	0.017	6.3×10^4	0.069	0.514
—	—	—	—	—	—	—	—	b^1_{384}	384	0.2	1	0.002	4.1×10^6	0.071	0.515
—	—	—	—	—	—	—	—	$b^{0.02}_{384}$	384	0.2	0.02	0.096	2.0×10^3	0.073	0.495
c^7_{96}	96	0.4	7.4	0.037	1.3×10^4	0.058	0.433	d^7_{96}	96	0.8	7.4	0.073	3.4×10^3	0.057	0.399
c^1_{96}	96	0.4	1	0.272	2.5×10^2	0.060	0.451	d^1_{96}	96	0.8	1	0.563	5.8×10^1	0.054	0.378
c^7_{192}	192	0.4	7.4	0.005	8.7×10^5	0.061	0.430	d^7_{192}	192	0.8	7.4	0.010	2.0×10^5	0.061	0.388
c^1_{192}	192	0.4	1	0.037	1.3×10^4	0.062	0.447	d^1_{192}	192	0.8	1	0.071	3.7×10^3	0.063	0.396
c^1_{384}	384	0.4	1	0.005	8.0×10^5	0.061	0.443	d^1_{384}	384	0.8	1	0.009	2.3×10^5	0.060	0.376
$c^{0.05}_{384}$	384	0.4	0.05	0.096	2.0×10^3	0.066	0.489	$d^{0.1}_{384}$	384	0.8	0.1	0.096	2.0×10^3	0.066	0.410
—	—	—	—	—	—	—	—	$d^{0.04}_{512}$	512	0.8	0.04	0.096	2.0×10^3	0.072	0.439
—	—	—	—	—	—	—	—	$\hat{d}^1_{384}$	384	0.8	1	0.096	1.9×10^3	0.064	0.397

TABLE 1. Navier–Stokes equations are integrated in a periodic domain $V_f = 4\pi \times 2\pi \times 2\pi$ with a resolution of $N_x \times N_y \times N_z$ Fourier modes, where $N_y = N_z = N_x/2$. The imposed mean shear $S = 0.5$ corresponds to a shear parameter $S^* = (L_0/L_S)^{2/3} = 7$, where $L_0 = u^3_{rms}/\epsilon$ denotes the integral scale and $L_S = \sqrt{\epsilon/S^3}$ is the shear scale with ϵ the mean dissipation rate. The r.m.s. velocity is defined as $u^2_{rms} = 2k/3$, where $k = 0.5\langle u_i u_i\rangle$ is the turbulent kinetic energy. Concerning the data at $Re_\lambda = 50$ with $\nu = 0.0125$, the Kolmogorov scale is $\eta = 0.07$ and shear scale $L_S = 0.84$ (referred to the uncoupled case, run a). The spectral resolution is $K_{max}\eta = 2.87$ to 15.5 i.e. $\eta/\Delta = 0.53$ to 2.8. Entries labelled with a hat refer to $Re_\lambda = 100$ with $\nu = 0.004$, $\eta = 0.03$, and $L_S = 0.7$ (referred to the uncoupled case, run $\hat{a}$). The spectral resolution is $K_{max}\eta = 4.97$, i.e. $\eta/\Delta = 0.92$. The Stokes number based on the Kolmogorov time is $St_\eta \simeq 1$, i.e. the particle relaxation time is $\tau_p = 0.4$ and $\tau_p = 0.25$ for the lower and higher Reynolds number cases respectively. The density ratio ρ_p/ρ_f is changed to achieve the desired mass load parameter $\Phi = M_p/M_f$, where $M_p = N_p\pi\rho_p d_p^3/6$ is the mass of the disperse phase (spheres with diameter d_p) and $M_f = \rho_f V_f$ is the mass of the carrier fluid. N_p denotes the number of particles and the ratio N_p/N_c is the mean number of particles per cell. The dataset is organized into four sections labelled a, b, c, d, corresponding to $\Phi = 0, 0.2, 0.4, 0.8$ respectively. The grid resolution is labelled by a subscript and the number of particles per cell by a superscript. The hat denotes higher Reynolds number simulations.

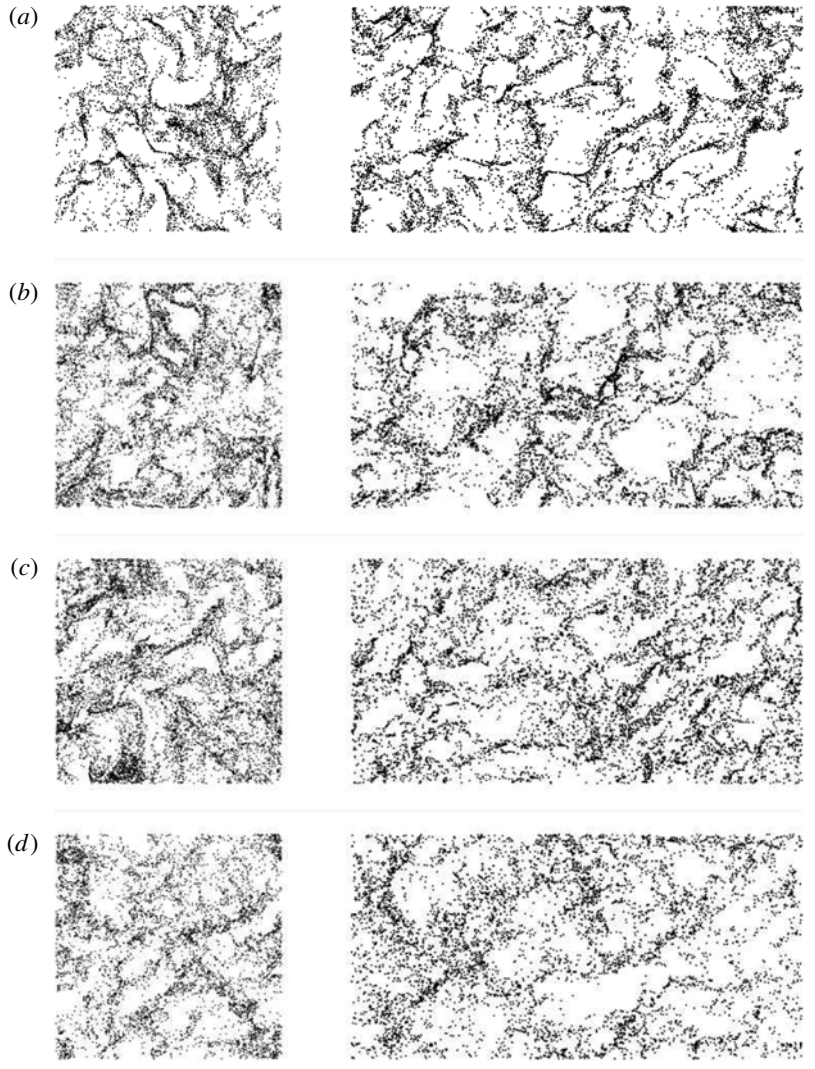


FIGURE 1. Snapshots of particle positions for increasing values of the mass load parameter Φ: (*a*) $\Phi = 0$, (*b*) $\Phi = 0.2$, (*c*) $\Phi = 0.4$ and (*d*) $\Phi = 0.8$. For all the datasets $St_\eta = 1$. Left column, thin slice in the y–z cross-flow plane; right column, slice in the x–y streamwise plane. The slice thickness is of the order of the Kolmogorov scale. The plots refer to cases a, b^1_{384}, c^1_{384}, d^1_{384}: see table 1.

Collins (1997). The behaviour of the RDF near the origin $g_{00}(r) \propto r^{-\alpha}$ is related to important geometric features of the clusters. In particular $\mathscr{D}_2 = 3 - \alpha$ is the so-called correlation dimension of the multi-fractal measure associated with the particle density (Grassberger & Procaccia 1983). A positive α indicates the occurrence of small-scale clustering.

The RDF is shown in figure 2(*a*) for the different values of the mass load parameter Φ (datasets a, b^1_{384}, c^1_{384} and d^1_{384} for a given grid resolution and mean particle number per cell). As the mass load increases, the data show the progressive attenuation of

https://doi.org/10.1017/jfm.2012.503 Published online by Cambridge University Press

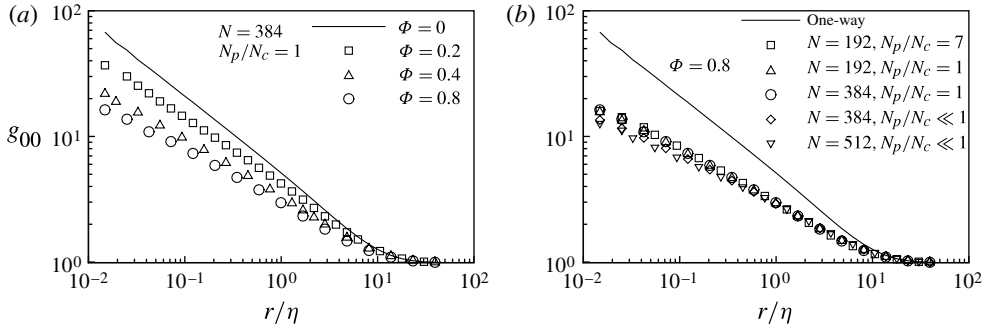


FIGURE 2. Projection of the ADF in the isotropic sector g_{00} as a function of separation. (*a*) Effect of an increasing mass load for a given resolution of the carrier phase, i.e. $384 \times 192 \times 192$ Fourier modes, and a fixed number of particles per cell, namely $Np/Nc = 1$: run *a* (—); run b^1_{384} (□); run c^1_{384} (△); run d^1_{384} (○). (*b*) Effect of the grid resolution and the mean number of particles per cell for a fixed value of the mass load $\Phi = 0.8$: run *a* (—); run d^7_{192} (□); run d^1_{192} (△); run d^1_{384} (○); run $d^{0.1}_{384}$ (◇); run $d^{0.04}_{512}$ (▽).

the small-scale particle concentration as measured by the scaling exponent α. The modification is substantial, as inferred from the small-scale values of g_{00} in the one-way coupling simulation (solid line) compared with the two-way coupling data at $\Phi = 0.8$ (open circles) that corresponds to the reduction by a factor of ~ 3.5 of the number of particle pairs. The statistical analysis confirms the impression gained by simple inspection of the particle patterns in figure 1, where clusters are definitely less defined at $\Phi = 0.8$ than at $\Phi = 0$ (figure 1*d* and figure 1*a* respectively). In any case clustering, though partially attenuated, is a persistent feature of the two-way coupling regime as measured by the exponent α. To exclude numerical artifacts, the numerical resolution and the mean particle number per cell have been changed systematically. Figure 2(*b*) gives the RDF for our largest mass load at $\Phi = 0.8$ in comparison with the reference dataset d^1_{384}. The RDF data show convergence with respect to both grid refinement and the mean particle number per cell, provided that $N_p/N_c \geqslant 1$. We conclude that clustering attenuation is the genuine physical consequence of the increased momentum exchange between carrier and disperse phase that takes place with increased mass loading.

In order to quantitatively deal with the strong anisotropy apparent in the visualizations of figure 1, we need to exploit the complete ADF shown in figure 3 as a contour plot on the unit sphere at separation $r \simeq 4\,\eta$ and different mass loads. In the plot, the ADF is normalized by its average, $g_{00}(4\,\eta)$. At small mass loads (the nearly one-way coupling regime), the ADF manifests a strong directionality with maxima aligned with the principal deformation axis of the mean flow. As the mass load is increased, i.e. moving from figure 3(*a*) to figure 3(*d*), progressive isotropization occurs.

The anisotropy of particle clusters can be better quantified at each scale by exploiting the directionality properties of the ADF. Its angular dependence $g(r, \hat{\boldsymbol{r}})$ can be resolved in terms of spherical harmonics,

$$g(r, \hat{\boldsymbol{r}}) = \sum_{j=0}^{\infty} \sum_{m=-j}^{j} g_{jm}(r) \mathrm{Y}_{jm}(\hat{\boldsymbol{r}}), \tag{3.2}$$

https://doi.org/10.1017/jfm.2012.503 Published online by Cambridge University Press

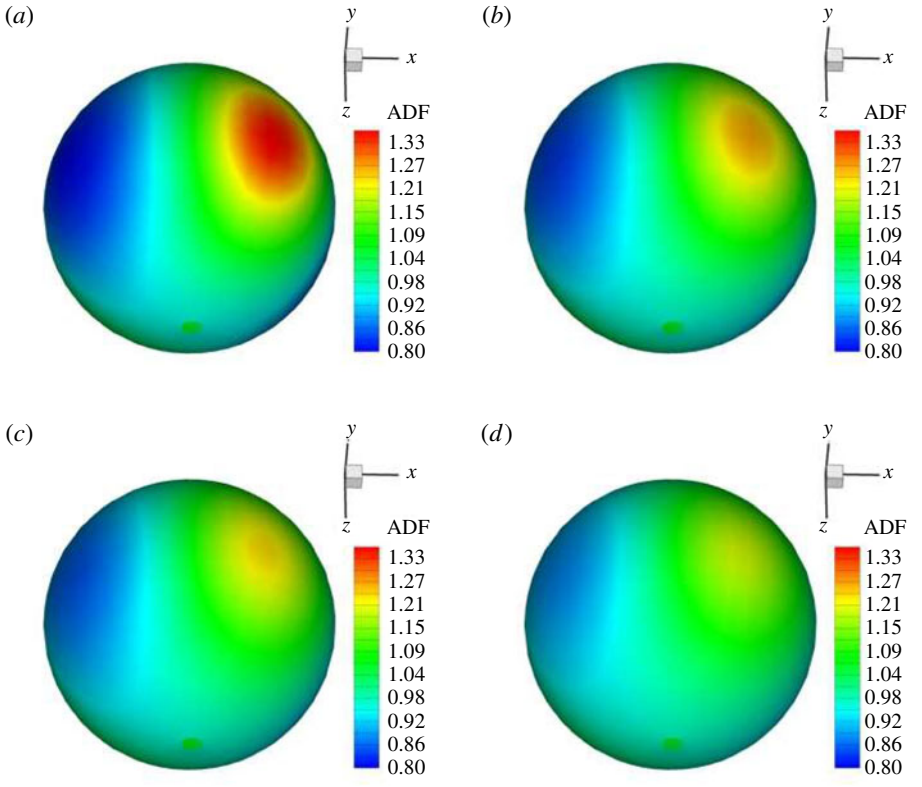


FIGURE 3. Contour plot of the ADF on the unit sphere. The ADF computed at separation 4η and normalized by its spherical average $g_{00}(4\eta)$ is shown for different mass loads: (*a*) $\Phi = 0$, run *a*; (*b*) $\Phi = 0.2$, run b^7_{192}; (*c*) $\Phi = 0.4$, run c^7_{192}; (*d*) $\Phi = 0.8$, run d^7_{192}.

achieving a systematic description both in terms of separation r, accounted for by the coefficients $g_{jm}(r)$, and directions, described by the shape of the basis functions $\mathrm{Y}_{jm}(\hat{\boldsymbol{r}})$. Figure 4 sketches the first few harmonics to highlight the geometric interpretation of the most significant projections. In the decomposition (3.2), the level of anisotropy increases with the index j.

In figure 5 we show the most energetic anisotropic projection of the ADF, namely g_{2-2}. As in the one-way coupling regime, by reducing the scale separation the intensity of the anisotropic projection increases, indicating directionality in the particle configurations. As Φ is increased (see the data in figure 5*a*), the exponent α_{2-2} describing the small-scale divergence of g_{2-2} is reduced, showing that the small-scale behaviour of $g_{2-2} \propto r^{\alpha_{2-2}}$ is controlled by the mass load ratio. In figure 5(*b*) we address the numerical convergence of g_{2-2}. The data show a trend consistent with that of the isotropic projection g_{00}. In brief, when the mean number of particles per cell is larger than or equal to one, the results are independent of the grid resolution, and a further increase of the ratio N_p/N_c does not produce any appreciable change.

To better understand the persistence of directionality at each scale, in figure 6(*a*) we show the ratio g_{2-2}/g_{00}. This indicator quantifies the scale-by-scale level of anisotropy of the particle configurations. The back-reaction on the carrier fluid partially reduces the small-scale anisotropy of the disperse phase. Indeed, in the interval of interest

https://doi.org/10.1017/jfm.2012.503 Published online by Cambridge University Press

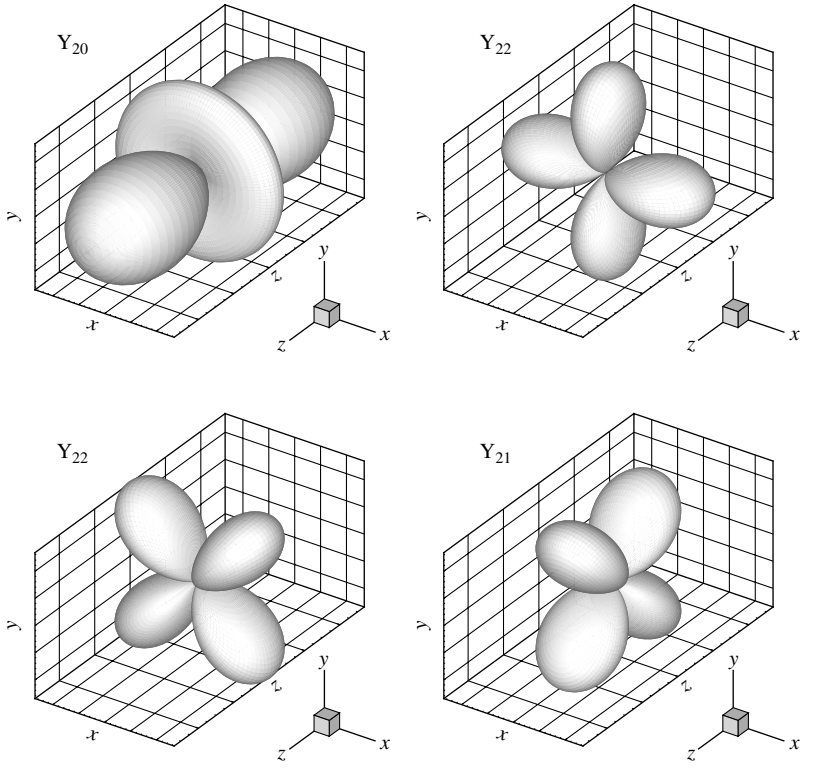


FIGURE 4. Sketch of the spherical harmonics in the sector $j = 2$. The harmonic Y_{22} selects the principal deformation directions of the mean flow $\boldsymbol{U} = Sx_2\,\boldsymbol{e}_1$ in the x_1–x_2 plane.

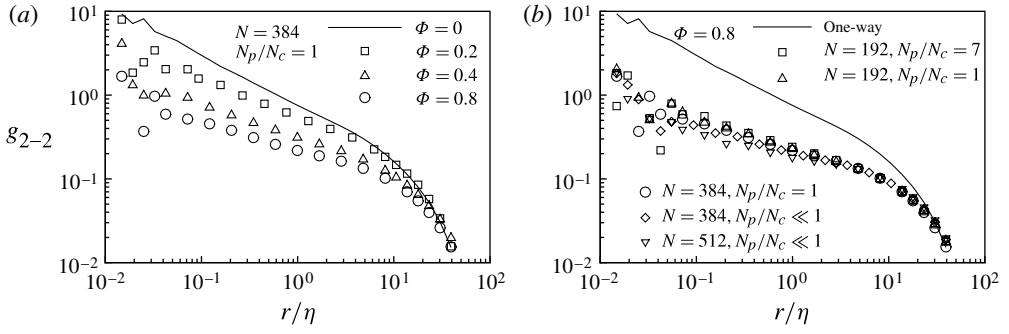


FIGURE 5. Projection of the ADF in the most energetic anisotropic sector $g_{2,-2}$ as a function of separation. (*a*) Effect of an increasing mass load for a given resolution of the carrier phase, i.e. $384 \times 192 \times 192$ Fourier modes, and a fixed number of particles per cell, namely $Np/Nc = 1$: run *a* (—); run b^1_{384} (□); run c^1_{384} (△); run d^1_{384} (○). (*b*) Effect of the grid resolution and the mean number of particles per cell at a fixed value of the mass load $\Phi = 0.8$: run *a* (—); run d^7_{192} (□); run d^1_{192} (△); run d^1_{384} (○); run $d^{0.1}_{384}$ (◇); run $d^{0.04}_{512}$ (▽).

centred around $r \sim \eta$, the local slope of g_{2-2}/g_{00} (symbols) progressively increases with the mass load (i.e. the ratio decreases faster at decreasing scale), in contrast to the saturation observed in the one-way coupling conditions (solid line). We stress that

https://doi.org/10.1017/jfm.2012.503 Published online by Cambridge University Press

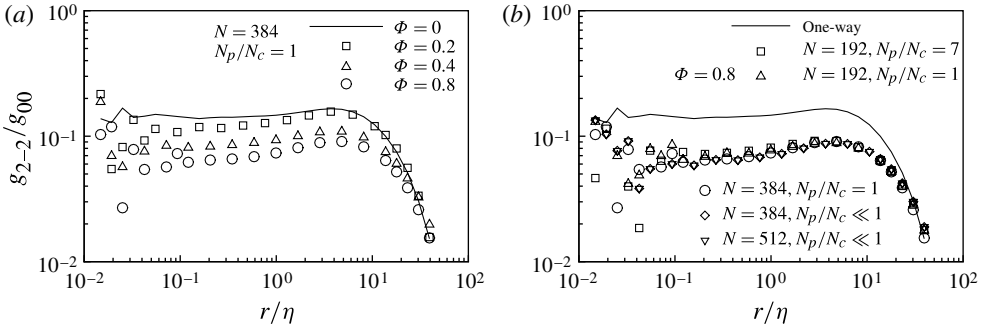


FIGURE 6. Normalized anisotropic projection of the ADF g_{2-2}/g_{00} as a function of separation. (*a*) Effect of an increasing mass load for a given resolution of the carrier phase, i.e. $384 \times 192 \times 192$ Fourier modes, and a fixed number of particles per cell, namely $Np/Nc = 1$: run *a* (—); run b^1_{384} (□); run c^1_{384} (△); run d^1_{384} (○). (*b*) Effect of the grid resolution and the mean number of particles per cell at a fixed value of the mass load $\Phi = 0.8$: run *a* (—); run d^7_{192} (□); run d^1_{192} (△); run d^1_{384} (○); run $d^{0.1}_{384}$ (◇); run $d^{0.04}_{512}$ (▽).

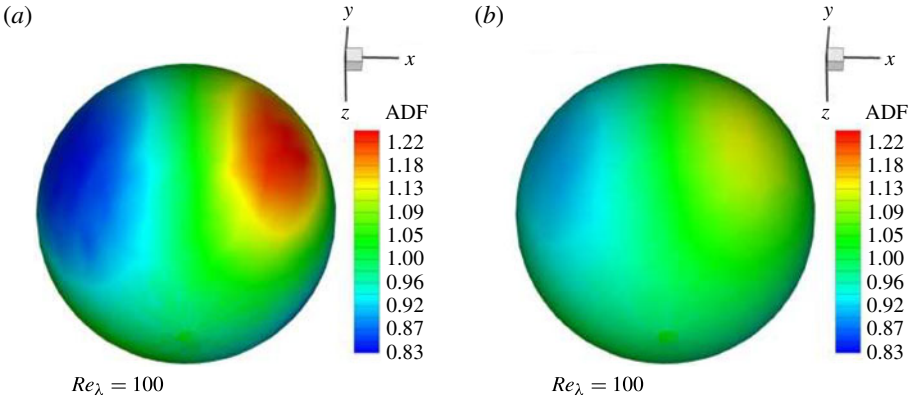


FIGURE 7. Contour plot of the ADF on the unit sphere. The ADF computed at separation 4η and normalized by its spherical average $g_{00}(4\eta)$ is shown for different mass loads: (*a*) $\Phi = 0$, run $\hat{a}$; (*b*) $\Phi = 0.8$, run $\hat{d}^1_{384}$.

also in the coupled cases the anisotropy of the clusters is significant, order 10 % of the total ADF amplitude. Although seemingly small, this amount will be shown (in § 4) to have a significant dynamic impact on turbulence modulation. Grid refinement tests on this observable are provided in figure 6(*b*), where g_{2-2}/g_{00} shows a well-defined convergence.

The analysis of anisotropic clustering under two-way coupling is completed in figures 7 and 8, where we address cases at higher Reynolds numbers (run $\hat{a}$ and $\hat{d}^1_{384}$ of table 1 at $Re_\lambda = 100$). The results show a weak dependence of cluster anisotropy on the Reynolds number even though the range of scales below L_S potentially available for isotropy recovery is now doubled. Indeed the ADF (figure 7) still indicates preferential alignment of the clusters. In figure 8(*a*) we address its g_{00} component, comparing the data at $\Phi = 0.8$ with corresponding data in the uncoupled case. As in

https://doi.org/10.1017/jfm.2012.503 Published online by Cambridge University Press

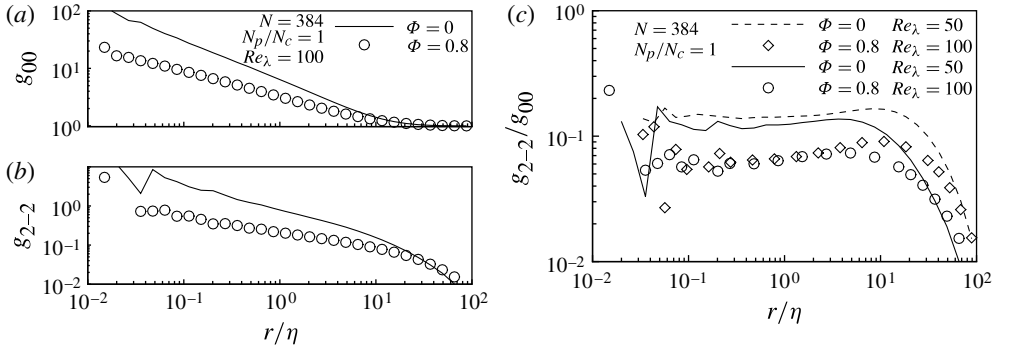


FIGURE 8. Projection of the ADF (*a*) in the isotropic sector g_{00}, (*b*) in the most energetic anisotropic sector $g_{2,-2}$, and (*c*) their ratio $g_{2,-2}/g_{00}$, as a function of separation for the higher Reynolds number ($Re_\lambda = 100$) data from run $\hat{a}$ (uncoupled case) and run $\hat{d}^1_{384}$ of table 1. In (*c*) data for the corresponding lower Reynolds number ($Re_\lambda = 50$) simulations, runs *a* and d^1_{384}, are also shown for comparison.

the lower Reynolds number case, the clustering intensity is depleted. In figure 8(*b*) we address g_{2-2}, which follows a similar trend. The ratio g_{2-2}/g_{00} at $\Phi = 0$ and 0.8 for both small and large Reynolds numbers confirms the substantial independence of the anisotropy of the clusters from the Reynolds number: see figure 8(*c*).

In conclusion, the overall behaviour of particle clusters is not substantially altered from the one-way coupling regime (Gualtieri *et al.* 2009), where the persistence of the clusters' directionality is observed up to the smallest viscous scales. The main difference due to the coupling is the slight reduction of clustering intensity and anisotropy as the mass load is increased.

4. Turbulence modulation

The following subsections address the alteration of turbulence due to the particles under progressive increase of the mass load ratio Φ. Specifically, we discuss the relationship between anisotropy of the fluid response and the geometry of the set where most particles concentrate, which corresponds to the support of the reaction field.

4.1. *Velocity fluctuations*

We start our description of turbulence modulation by observing that, in homogeneous shear flow, the mean velocity profile is imposed. This excludes its modification by the particles, which is instead an important feature of channels or jet flows. Indeed, in homogeneous shear flow the entire effect of the coupling occurs at the level of the velocity fluctuations. Hence the basic quantities to be addressed are single-point statistics.

The turbulent kinetic energy, normalized by its value in the uncoupled case, k/k_0, is addressed in figure 9(*a*) as a function of the mass load ratio Φ. In the figure, data obtained with different grid resolutions and mean number of particles per cell are compared to check convergence. As a general trend, the turbulent fluctuations are progressively attenuated by increasing the mass load ratio, consistent with previous findings in isotropic turbulence and wall-bounded shear flows. The turbulent kinetic

https://doi.org/10.1017/jfm.2012.503 Published online by Cambridge University Press

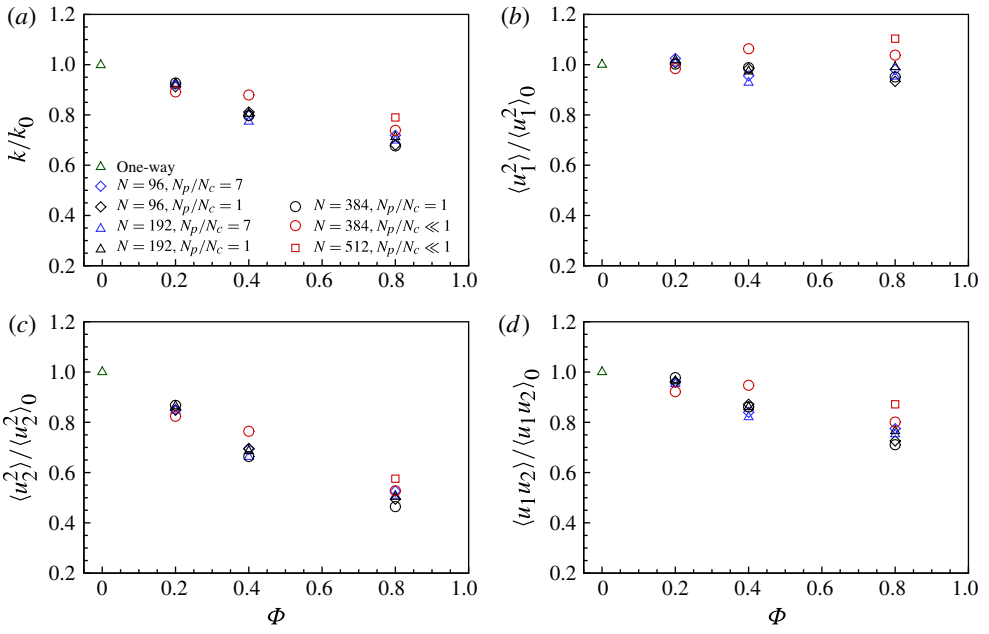


FIGURE 9. Effect of the mass load Φ on the turbulent fluctuations. Data normalized with the corresponding values of the uncoupled case: (*a*) turbulent kinetic energy $k = 1/2\langle u_i\, u_i\rangle$; (*b*) longitudinal velocity variance $\langle u_1^2\rangle$; (*c*) transverse velocity variance $\langle u_2^2\rangle$; (*d*) Reynolds shear stress $-\langle u_1\, u_2\rangle$. The symbol shape corresponds to the carrier fluid resolution, i.e. $96 \times 48 \times 48$ ($\diamond$), $192 \times 96 \times 96$ ($\triangle$), $384 \times 192 \times 192$ ($\bigcirc$), $512 \times 256 \times 256$ ($\square$) Fourier modes. Different colours label the number of particles per cell: $N_p/N_c = 7.4$ (blue), $N_p/N_c = 1$ (black), $N_p/N_c \ll 1$ (red).

energy converges with respect to grid refinement and mean particle number per cell, provided that $N_p/N_c \geqslant 1$.

The normalized streamwise and transverse fluctuations, $\langle u_1^2\rangle/\langle u_1^2\rangle_0$ and $\langle u_2^2\rangle/\langle u_2^2\rangle_0$, respectively, are shown in figure 9(*b*,*c*) to document the large-scale anisotropy of the carrier phase. At variance with the turbulent kinetic energy, $\langle u_1^2\rangle$ is less sensitive to the mass load. It is worth stressing that the trend of $\langle u_1^2\rangle$ versus Φ may look contradictory at first sight. Indeed, convergence plays a significant role here: at $N_p/N_c < 1$ a slight increase of streamwise fluctuations with the mass load is observed. The proper prediction from the present two-way coupling model is, however, the opposite (i.e. decrease of fluctuation with mass loading), as shown by the converged simulations with $N_p/N_c \geqslant 1$: for instance, compare triangles (192 streamwise modes) of different colours, namely black ($N_p/N_c = 1$) and blue ($N_p/N_c = 7$).

The normalized transverse velocity fluctuations $\langle u_2^2\rangle/\langle u_2^2\rangle_0$ are shown in figure 9(*c*). A clear trend towards attenuation consistently emerges, with the spanwise data $\langle u_3^2\rangle$(not shown) substantially reproducing $\langle u_2^2\rangle$. The reduction of the turbulent kinetic energy is indeed associated with the depletion of the two cross-flow variances, up to 50 % at $\Phi = 0.8$. The selective alteration of the cross-flow velocity components with respect to the streamwise fluctuation is the footprint of large-scale flow anisotropy enhancement. The Reynolds shear stress (figure 9*d*) is strongly depleted (20 to 30 %) under large mass loads, leading to a corresponding reduction of turbulent kinetic energy production.

https://doi.org/10.1017/jfm.2012.503 Published online by Cambridge University Press

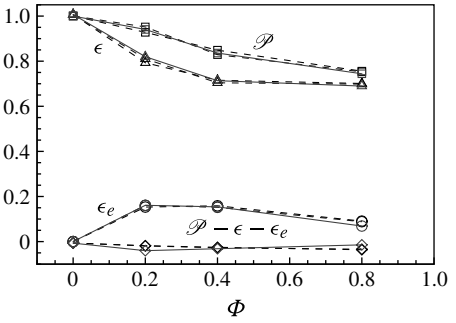


FIGURE 10. Turbulent kinetic energy budget. Data normalized with the production rate of the uncoupled case $\mathscr{P}_0$: production $\mathscr{P}$ (□), viscous energy dissipation ϵ (△), and energy flux intercepted by particles ϵ_e (○). The algebraic sum $\mathscr{P} - \epsilon - \epsilon_e$ is also shown (◇), to check the quality of the budget. Data from runs b^7_{192}, c^7_{192}, d^7_{192} (dashed blue line), runs b^1_{192}, c^1_{192}, d^1_{192} (dot-dashed black line) and runs b^1_{384}, c^1_{384}, d^1_{384} (dotted red line) provide the sensitivity of the budget to the numerical resolution and the number of particles per cell.

4.2. *Turbulent kinetic energy budget*

The turbulent kinetic energy budget is straightforward in the uncoupled case where the production term $\mathscr{P}_0 = -S\,\langle u_1\,u_2\rangle_0$ balances the viscous dissipation ϵ_0 (the subscript stands for $\Phi = 0$). The budget, $\mathscr{P} - \epsilon - \epsilon_e = 0$, involves a new term in the two-way coupling regime, namely the energy exchange $\epsilon_e = -\langle \sum_p \boldsymbol{F}_p \cdot \boldsymbol{u}_p \rangle$ between the two phases due to the Stokes drag, with $\boldsymbol{u}_p$ the fluid velocity at the particle position and $\boldsymbol{F}_p = -m_p/\rho_f \boldsymbol{f}_p$ the force exerted by the fluid on the particle normalized by the fluid density: see § 2. In fact, in steady conditions the average particle kinetic energy is constant, $\mathrm{d}\langle \sum_p m_p\,|\boldsymbol{v}_p|^2\,/2\rangle/\mathrm{d}t = 0$, i.e. $\langle \sum_p m_p \boldsymbol{f}_p \cdot \boldsymbol{v}_p \rangle = 0$. It follows that $\epsilon_e = -\langle \sum_p \boldsymbol{F}_p \cdot \boldsymbol{u}_p \rangle = -\langle \sum_p \boldsymbol{F}_p \cdot (\boldsymbol{u}_p - \boldsymbol{v}_p) \rangle > 0$ since $\boldsymbol{F}_p = -3\pi d_p \nu\,(\boldsymbol{u}_p - \boldsymbol{v}_p)$, implying that the total kinetic energy (fluid and particles) is globally dissipated by the viscous stress and the Stokes drag: see Sundaram & Collins (1999). The energy provided by the Reynolds shear stress is partially intercepted by the back-reaction through the energy exchange term ϵ_e and then dissipated by the disperse phase by means of the Stokes drag. The energy exchange term feeds an alternative dissipation channel working in parallel with viscosity. This is indeed a common feature of flows with microstructure: see Casciola & De Angelis (2007) for a similar mechanism in the context of polymer-laden flows. The energy budget is addressed in graphical form in figure 10. The considerable reduction of the production rate, discussed in connection with the alteration of the Reynolds shear stress, entails the reduction of the viscous dissipation ϵ. The energy exchange ϵ_e is typically smaller than ϵ and, interestingly, achieves its maximum – order 15 % of $\mathscr{P}_0$ – at intermediate mass loads (circles in figure 10). The sensitivity analysis to refinement of grid resolution and mean number of particles per cell confirms the consistency of the results.

4.3. *Energy spectra*

The radial energy spectrum for the reference cases a, b^7_{192}, c^7_{192} and d^7_{192} is shown in log scale in figure 11(a). As Φ increases, turbulent fluctuations are progressively attenuated in an intermediate range of scales and enhanced at small scales, down to the dissipative scale of the flow. The effect can be better appreciated in figure 11(b), which shows the ratio $E_{\Phi=0}/E_\Phi$ versus wavenumber, where the energy depletion of

https://doi.org/10.1017/jfm.2012.503 Published online by Cambridge University Press

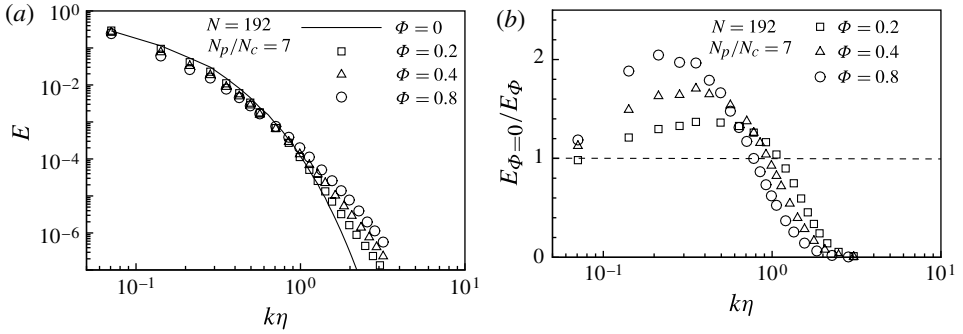


FIGURE 11. Effect of the mass load on the energy spectra for a fixed spectral resolution of the carrier phase and a given number of particles per cell. Data for the one-way coupled simulation run a (—) are compared with two-way coupled simulations for increasing mass loads: $\Phi = 0.2$, run b^7_{192} (□); $\Phi = 0.4$, run c^7_{192} (△); $\Phi = 0.8$, run d^7_{192} (○) (see table 1). (a) Direct comparison of the energy spectra. (b) Ratio $E_{\Phi=0}/E_\Phi$ in linear-log scale.

the largest scales (up to a factor of two) and the substantial augmentation of the smallest scales is apparent. The net effect on the turbulent kinetic energy is the already observed overall reduction.

The large/intermediate-scale depletion of energy and the small-scale enhancement determines a cross-over wavenumber where the spectrum of the particle-laden flow intercepts the reference spectrum in the absence of back-reaction (pivot wavenumber). In the point particle approximation the dimensionless pivot wavenumber $k_{pivot}\eta$ may only depend on the mass load Φ, the Stokes number St_η, and the Reynolds number Re_λ. We recall that the dependence on the particle Reynolds number $Re_p = d_p\langle(\boldsymbol{w}_p \cdot \boldsymbol{w}_p)^2\rangle^{1/2}/\nu$ ($\boldsymbol{w}_p$ is the fluid–particle relative velocity) is ruled out by the point particle assumption. At any rate Re_p can be *a posteriori* computed by measuring a typical slip velocity and by assuming a solid–fluid density ratio ρ_p/ρ_f. For given Stokes number ($St_\eta \sim 1$) and Reynolds number ($Re_\lambda \sim 50$), density ratios taken from table 1 give $Re_p = 10^{-2}$ to 10^{-1}, confirming the appropriateness of the point particle approximation for the parameter range investigated here. Moreover, in most cases, the mean particle distance $\lambda_p = d_p\sqrt[3]{\pi\rho_p/(6\,\rho_f\,\Phi)} \in [5, 220]d_p$ is sufficiently large to justify the neglect of inter-particle interactions. In these conditions, a slight dependence of the pivot wavenumber on the mass load, with typical values ranging from $k_{pivot}\eta = 11$ to 8, changing Φ from 0.2 to 0.8, emerges from the fixed St_η and Re_λ data of figure 11(b). It is worth stressing that similar pivoting behaviour has recently been observed in turbulent flows laden with finite-size particles: see e.g. Gao *et al.* (2011). The authors concluded that the pivot wavenumber depends on both the particle diameter and the particle-to-fluid density ratio. In our present case, instead, the cross-over has a different origin. In our simulations, where actual particle size and density ratio are irrelevant, the pivoting of the energy spectra is most probably due to a collective effect of the clusters.

Figure 12(a) shows the spectral distribution of the turbulent shear stress (cospectrum). Although hardly appreciable in log scale, the cospectrum slightly decreases at large scales as the mass load ratio increases, consistent with the overall reduction of the shear stress. Meanwhile, the range of scales that mostly contribute to the Reynolds stress progressively broadens with respect to the case $\Phi = 0$, only slightly at $\Phi = 0.2$ and more markedly at larger mass loads: see the symbols versus

https://doi.org/10.1017/jfm.2012.503 Published online by Cambridge University Press

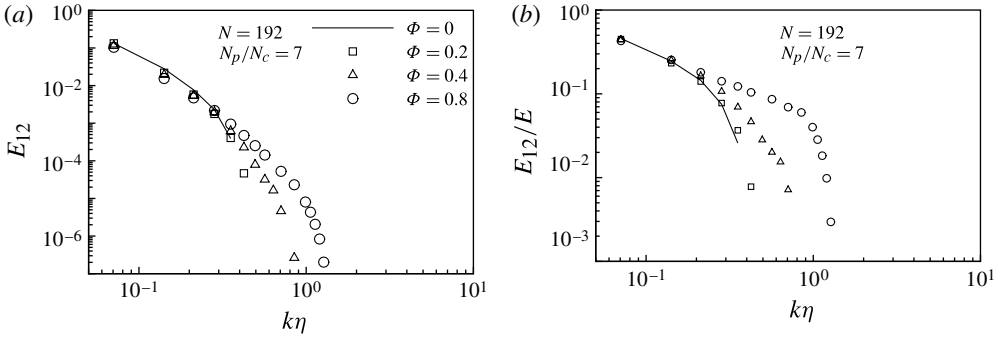


FIGURE 12. Effect of the mass load on the energy cospectra for a fixed spectral resolution of the carrier phase and a given number of particles per cell. Data for the one-way coupled simulation run a (—) are compared with two-way coupled simulations for increasing mass loads Φ: $\Phi = 0.2$, run b^7_{192} (□); $\Phi = 0.4$, run c^7_{192} (△); $\Phi = 0.8$, run d^7_{192} (○) (see table 1). (a) Direct comparison of the energy cospectra. (b) Ratio of the energy cospectrum and the energy spectrum E_{12}/E for the same datasets as in (a).

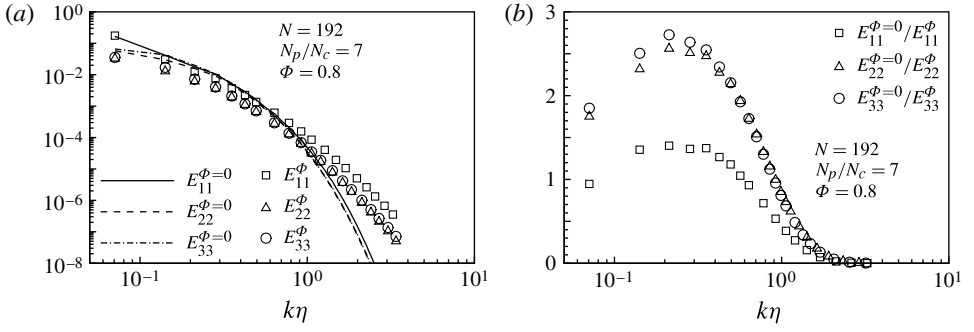


FIGURE 13. (a) Energy spectrum of the three velocity components. Data for the one-way coupled simulation run a (lines) are compared against corresponding data for the two-way coupling regime, namely run d^7_{192}. Uncoupled case: longitudinal component E_{11} (solid line), transverse component E_{22} (dashed line), spanwise component E_{33} (dot-dashed line). Two-way coupling run d^7_{192}: E_{11} (□), E_{22} (△), E_{33} (○). (b) Ratio between the longitudinal, transverse and spanwise energy spectra in the uncoupled case and the corresponding spectra in the two-way coupling regime from run d^7_{192}.

the solid line in the figure. Since the energy production rate is proportional to the cospectrum, $-SE_{12}(k)$, the dynamic consequence is the corresponding enlargement of the energy injection range $k_0 = 2\pi/L_0 < k < k_S = 2\pi/L_S$. Indeed, the shear scale L_S reduces as much as 20 % at the highest mass load with respect to the uncoupled case, as can be inferred from table 1 and the definition $L_S = \sqrt{\epsilon/S^3}$. Figure 12($b$) addresses the ratio between cospectrum and spectrum. This ratio characterizes the anisotropy pertaining to each scale: see Saddoughi & Veeravalli (1994). The increase of the mass load apparently increases the anisotropy of the smallest scales: see e.g. the data at $\Phi = 0.8$.

The energy repartition among the three velocity components (E_{11}, longitudinal component; E_{22}, transverse; E_{33}, spanwise) is provided in figure 13(a) for $\Phi = 0.8$. A preferential alteration of the three energy contributions is observed. The effect is better

https://doi.org/10.1017/jfm.2012.503 Published online by Cambridge University Press

visualized in figure 13(*b*), where the ratio $E_{ii}^{\Phi=0}/E_{ii}^{\Phi}$ (no sum on the index i) is shown for each component. The alteration is selective: the cross-flow velocity components are damped by a factor of 2.5 in the intermediate range of scales and amplified at the smallest scales. At large/intermediate scales, the longitudinal component is less affected by the particles than the cross-flow components (depletion of a factor of 1.4 compared to 2.5). The augmentation at small scales is instead larger, as indicated by the smaller ratio $E_{11}^{\Phi=0}/E_{11}^{\Phi=0.8}$ compared to $E_{22}^{\Phi=0}/E_{22}^{\Phi=0.8}$.

4.4. *Spectral distribution of the back-reaction*

In spectral space, the interphase momentum coupling is described by the Fourier transform of the correlation $\Psi_{ij}(k) = \mathscr{F}\langle F_i(\boldsymbol{x})\, u_j(\boldsymbol{x}+\boldsymbol{r})\rangle$ between back-reaction $\boldsymbol{F}$ and fluid velocity. $\Psi = \Psi_{ii}$ forces the energy spectrum E according to the equation

$$\frac{\partial E(k)}{\partial t} = T(k) + P(k) - D(k) + \Psi(k), \tag{4.1}$$

with T the energy transfer term, $P = -SE_{12}$ the production, and $D = 2\nu k^2 E$ the dissipation spectrum, where the time derivative in the left-hand side vanishes at steady state. A preliminary understanding of the spectral properties of the coupling term $\Psi(k)$ is readily provided under the assumption that the particle relaxation time is small, so that the particle back-reaction field in physical space can be approximated by

$$\boldsymbol{F}(\boldsymbol{x}) = -\sum_{p=1}^{N_p} \frac{m_p}{\rho_f}\left[\frac{\boldsymbol{v}(\boldsymbol{x}_p) - \boldsymbol{v}^p}{\tau_p}\right]\delta(\boldsymbol{x}-\boldsymbol{x}_p) \simeq -\sum_{p=1}^{N_p}\frac{m_p}{\rho_f}\frac{\mathrm{D}\boldsymbol{v}(\boldsymbol{x}_p)}{\mathrm{D}t}\delta(\boldsymbol{x}-\boldsymbol{x}_p). \tag{4.2}$$

Its Fourier transform is

$$\hat{\boldsymbol{F}}(\boldsymbol{k}) \propto \frac{1}{(2\pi)^3}\int \frac{\mathrm{D}\boldsymbol{v}(\boldsymbol{y})}{\mathrm{D}t} c(\boldsymbol{y}) \mathrm{e}^{-\mathrm{i}\boldsymbol{k}\cdot\boldsymbol{y}}\,\mathrm{d}^3\boldsymbol{y} = \int \widehat{\frac{\mathrm{D}\boldsymbol{v}}{\mathrm{D}t}}(\boldsymbol{k}_1)\hat{c}(\boldsymbol{k}-\boldsymbol{k}_1)\,\mathrm{d}^3\boldsymbol{k}_1, \tag{4.3}$$

where $c(\boldsymbol{y}) = \sum_p \delta(\boldsymbol{y}-\boldsymbol{x}_p)$ is the instantaneous (microscopic) concentration of the point particles. The field $\Psi(k)$ is essentially the spherical average of $\langle \hat{\boldsymbol{F}}(\boldsymbol{k})\cdot\hat{\boldsymbol{v}}^{\dagger}(\boldsymbol{k})\rangle + \text{c.c.}$, with

$$\langle \hat{\boldsymbol{F}}(\boldsymbol{k})\cdot\hat{\boldsymbol{v}}^{\dagger}(\boldsymbol{k})\rangle \propto \int \left\langle \widehat{\frac{\mathrm{D}\boldsymbol{v}}{\mathrm{D}t}}(\boldsymbol{k}_1)\hat{c}(\boldsymbol{k}-\boldsymbol{k}_1)\cdot\hat{\boldsymbol{v}}^{\dagger}(\boldsymbol{k})\right\rangle \mathrm{d}^3\boldsymbol{k}_1. \tag{4.4}$$

This expression shows a sort of triadic interaction between the fields of fluid velocity, fluid acceleration, and instantaneous particle concentration. Such interaction is strongly non-local in Fourier space when the instantaneous particle concentration is spatially intermittent with clusters of local high density separated by void regions. Observe that the effect emerges as an average of vertex interactions of the instantaneous fields, which are indeed those that carry the intermittency. When the instantaneous concentration field is non-compact in Fourier space (as happens in the presence of clustering) it allows for the coupling of small and large scales of the system as a consequence of the collective behaviour of the particle swarms. Given the highly nonlinear nature of $\Psi(k)$, the use of DNS data is mandatory.

The energy removal from the large scales of the fluid motion and the injection at the small scales is apparent in figure 14(*a*), where $\Psi(k)$ is plotted for different mass loads. This is consistent with the observed depletion of the turbulent kinetic energy spectrum at intermediate scales and with its augmentation at the smallest ones. More

https://doi.org/10.1017/jfm.2012.503 Published online by Cambridge University Press

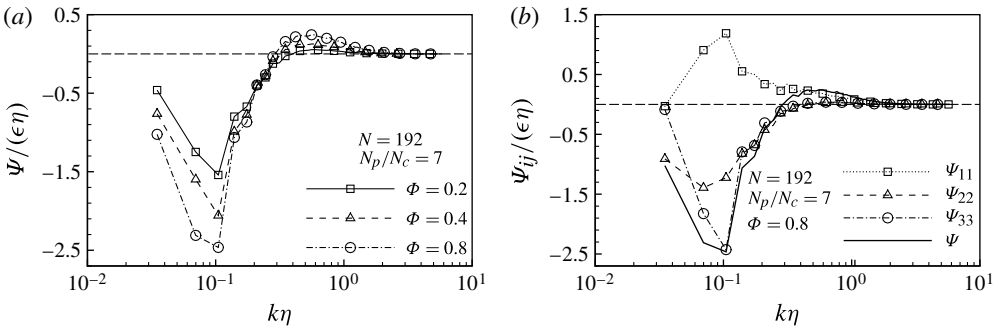


FIGURE 14. Spectral distribution of the back-reaction coupling term. (*a*) Forcing term Ψ as a function of wavenumber under different coupling conditions. (*b*) Different projections of the coupling term for a fixed mass load $\Phi = 0.8$.

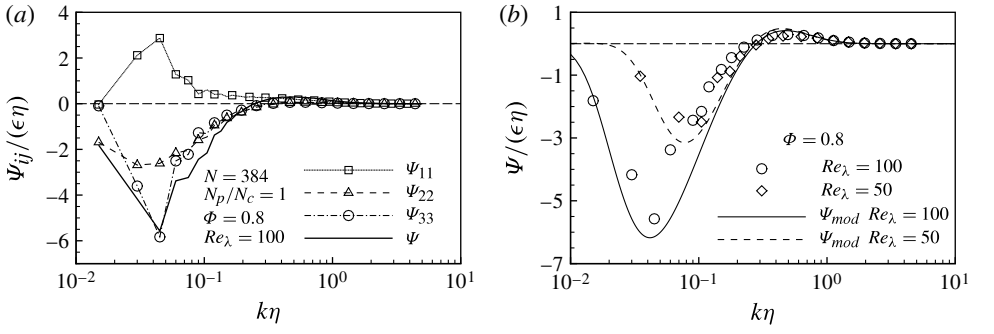


FIGURE 15. Spectral distribution of the back-reaction coupling term. (*a*) Different projections of the coupling term for a fixed mass load $\Phi = 0.8$ at $Re_\lambda = 100$. (*b*) The data at $Re_\lambda = 50$ ($\diamond$) and $Re_\lambda = 100$ ($\bigcirc$) are compared with the prediction of the model given by (4.5) for the two values of the Reynolds number, dashed and solid line respectively.

interesting is figure 14(*b*) where, for a fixed value of the mass load $\Phi = 0.8$, we present the three contributions to Ψ. It turns out that Ψ_{11} is always positive, meaning that the streamwise velocity fluctuations are forced at all scales by the Stokes drag. In contrast, the transverse components, Ψ_{22} and Ψ_{33}, are always negative. It is only by adding the three contributions that two distinct ranges of scales emerge where energy is respectively depleted and enhanced. The physical interpretation is that the Stokes drag intercepts energy from the fluid turbulence at intermediate scales and depletes the velocity fluctuations. The intercepted energy is partly pumped back to the fluid at small scales, increasing the energy content by orders of magnitude: compare the solid line (one-way coupling) and open symbols (two-way coupling) in figure 11(*a*).

The same analysis is repeated in figure 15(*a*) for a higher Reynolds number, $Re_\lambda = 100$, showing that the overall picture does not change with respect to the $Re_\lambda = 50$ case discussed so far. More information is gained by direct comparison of the two cases: figure 15(*b*). The position of the negative peak at small wavenumber moves towards larger scales as the Reynolds number increases. The effect is interesting. It shows that the alteration of the energy-containing range is a genuine effect of the momentum coupling rather than a spurious result of insufficient scale

https://doi.org/10.1017/jfm.2012.503 Published online by Cambridge University Press

separation between large turbulent scales and particle clusters, as might have been suspected given the relatively low Reynolds number of the present simulations. Deeper understanding is gained by addressing a physical model of the back-reaction in spectral space. Following Druzhinin (2001), the back-reaction term may be modelled as

$$\Psi_{mod}(k) = \frac{\Phi}{1+\Phi} D(k) \left[1 - \alpha St_\eta \frac{k\, E(k)}{u_\eta^2} \right], \tag{4.5}$$

where u_η is the Kolmogorov velocity and α is a constant of the model that can be determined by prescribing the particle dissipation rate $\epsilon_e = -\int \Psi(k)\, \mathrm{d}^3k$. In (4.5) the first term, $\Phi/(1+\Phi)D$, being proportional to the dissipation spectrum, accounts for the reduction of viscous dissipation rate due to the particles: see e.g. Druzhinin & Elghobashi (1999). In fact, for $\alpha = 0$ we get $-D(k) + \Psi(k) \simeq -(1-\Phi)D(k)$, corresponding to an effective decrease of viscosity proportional to the mass loading. The second term, proportional to αSt_η, has the opposite sign and accounts for the finite inertia effects of the particles: see Druzhinin (1995). This model helps us to understand the effects observed in the present simulations. After fitting the data with the Pao spectrum $E(k) = C_k \epsilon^{2/3} k^{-5/3} f_L(kL_0) f_\eta(k\eta)$ where $f_L = \{kL_0/\,[(kL_0)^2 + c_L]^{1/2}\}^{11/3}$ and $f_\eta = \exp\{-\beta\{[(k\eta)^4 + c_\eta^4]^{1/4} - c_\eta\}\}$ (see e.g. Pope 2000), the model spectrum is used to evaluate Ψ via (4.5). The result of the procedure is shown in figure 15(*b*) (lines) for the two Reynolds number values. The agreement with the raw data is remarkable, and gives us confidence to exploit the model to understand the coupling term at larger Reynolds number. The location of the minimum, $k_{min}\eta$, can be estimated as $k_{min}\eta = \sqrt{21 c_L / Re^{3/2}}$, where c_L is a Reynolds-independent constant controlling the energy-containing range of the Pao spectrum and $Re = (L_0/\eta)^{4/3}$. It follows that, according to the model, the negative peak occurs at $L_{min} = 2\pi/\sqrt{21 c_L} L_0$, a scale which is directly proportional to the integral scale of the flow L_0. This implies that as the Reynolds number increases the energy removal range remains locked to the integral scale, i.e. it is indeed a large-scale feature of the coupled particle–fluid interaction, consistent with the indications of our moderate Reynolds number data.

4.5. *Spectral resolution issues*

We conclude our analysis by addressing the effects of grid resolution and mean number of particles per cell on the spectra. The results are summarized in figure 16, where the spectrum for two mass loads, $\Phi = 0.2$ and $\Phi = 0.8$, are shown in figure 16(*a,b*), respectively. The energy cospectrum is plotted in the two insets. Three resolutions are considered, namely $96 \times 48 \times 48$ (coarse, diamonds), $192 \times 96 \times 96$ (intermediate, triangles) and $384 \times 192 \times 192$ (fine, circles). For each case two mean particle numbers per cell are addressed, namely $N_p/N_c = 7.4$ (blue symbols), $N_p/N_c = 1$ (black symbols) and, for the finest grid only, $N_p/N_c \ll 1$ (red symbols). The energy spectrum and cospectrum are observed to converge in the range of scales shared by the different datasets whenever $N_p/N_c \geqslant 1$. Below one particle per cell the results are unreliable due to the back-reaction becoming progressively too spotty. The dissipation spectrum plotted in figure 16(*c,d*) provides details of the smallest scales, where convergence is apparent for $N_p/N_c \geqslant 1$. The inset shows the data in a log-linear scale to better evaluate the energy dissipation rate corresponding to the area below the curve.

https://doi.org/10.1017/jfm.2012.503 Published online by Cambridge University Press

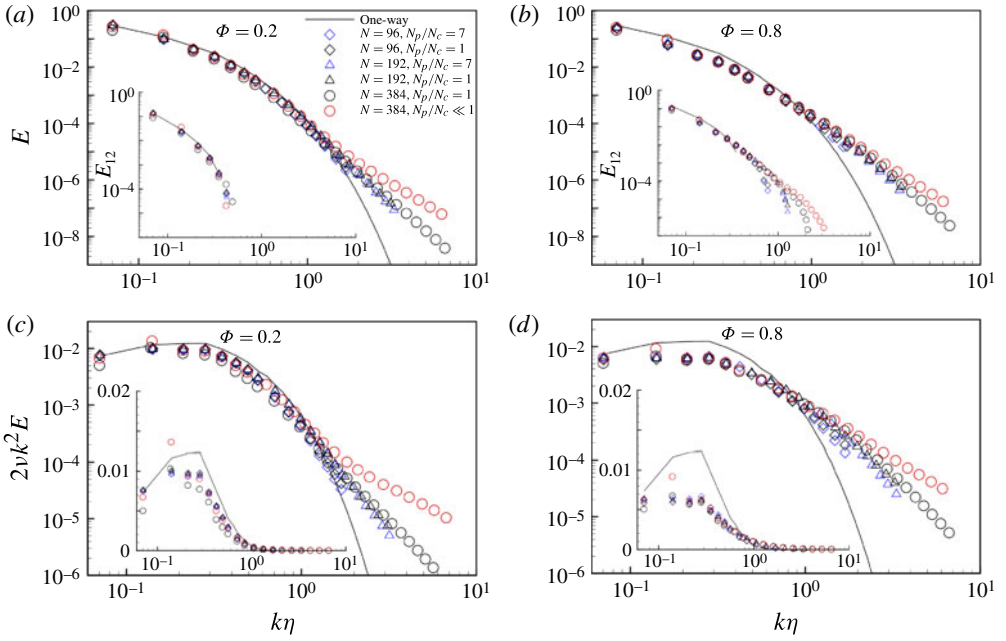


FIGURE 16. Effect of the grid resolution and of the number of particles per cell at a fixed value of the mass load. (*a*,*b*) The energy spectrum and cospectrum (inset) at (*a*) $\Phi = 0.2$ and (*b*) $\Phi = 0.8$. (*c*,*d*) The energy dissipation spectrum at (*c*) $\Phi = 0.2$ and (*d*) $\Phi = 0.8$. In the insets the same data are shown in a semi-logarithmic scale to better appreciate the convergence of the energy dissipation. The symbol shape corresponds to the carrier fluid resolution, i.e. $96 \times 48 \times 48$ ($\diamond$), $192 \times 96 \times 96$ ($\triangle$) and $384 \times 192 \times 192$ ($\bigcirc$) Fourier modes. Different colours label the number of particles per cell: $N_p/N_c = 7.4$ (blue), $N_p/N_c = 1$ (black), $N_p/N_c \ll 1$ (red).

In conclusion, the analysis exploited in figure 16 allows us to exclude numerical artifacts, even for the statistics of the dissipative scales that are well captured when $d_p < \Delta < \eta$ and $N_p/N_c \geqslant 1$.

4.6. *Anisotropy*

The discussion of the results needs to be completed by addressing the system anisotropy. Concerning the large scales, the anisotropy is quantified by the deviatoric component of the Reynolds stress tensor $b_{ij} = \langle u_i\, u_j\rangle / \langle u_k\, u_k\rangle - 1/3\delta_{ij}$. Since anisotropy is already present in the uncoupled case, to isolate the effect of the back-reaction we address the ratio $\|\boldsymbol{b}\|/\|\boldsymbol{b}\|_0$ in figure 17(*a*) (the subscript stands for $\Phi = 0$, and $\|\boldsymbol{b}\| = \sqrt{b_{ij}\, b_{ij}}$). The anisotropy enhancement mainly results from the combined attenuation of the cross-flow variances, $\langle u_2^2\rangle$ and $\langle u_3^2\rangle$, and the substantial reduction of the Reynolds shear stress $-\langle u_1 u_2\rangle$, with a slight modification of the longitudinal fluctuation $\langle u_1^2\rangle$. The ratio $\|\boldsymbol{b}\|/\|\boldsymbol{b}\|_0$ increases significantly with increasing mass load.

At small dissipative scales, anisotropy can be quantified by the norm, $\|\boldsymbol{a}\| = \sqrt{a_{ij}\, a_{ij}}$, of the deviatoric component, $a_{ij} = \epsilon_{ij}/\epsilon_{kk} - 1/3\delta_{ij}$, of the pseudo-dissipation tensor $\epsilon_{ij} = 2\,\nu\langle \partial_k u_i\, \partial_k u_j\rangle$. The quantity $\|\boldsymbol{a}\|/\|\boldsymbol{a}\|_0$ is shown by open circles in figure 17(*a*) in comparison with the large-scale anisotropy indicator $\|\boldsymbol{b}\|/\|\boldsymbol{b}\|_0$ (open squares). The data show a dramatic growth of the gradient anisotropy which increases up to 300 % with respect to the reference uncoupled case. Momentum coupling of fluid and

https://doi.org/10.1017/jfm.2012.503 Published online by Cambridge University Press

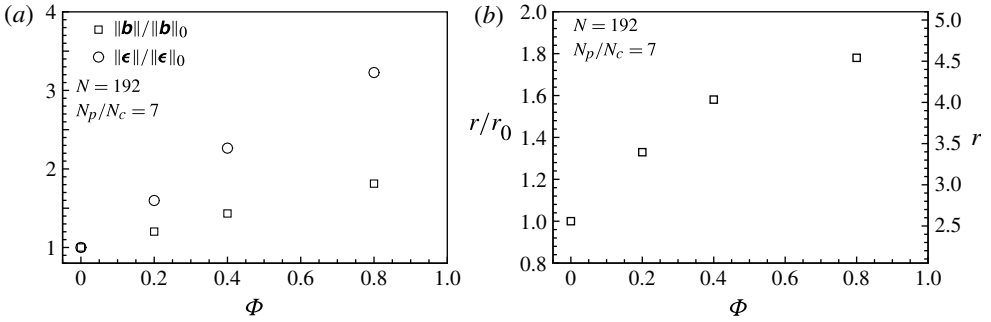


FIGURE 17. (*a*) Normalized norm of the deviatoric component of the Reynolds stress tensor $\|\boldsymbol{b}\|/\|\boldsymbol{b}\|_0$ (□) and of the pseudo-dissipation tensor $\|\boldsymbol{a}\|/\|\boldsymbol{a}\|_0$ (○) as a function of the mass load ratio Φ. (*b*) Ratio $r = \|\boldsymbol{a}\|/\|\boldsymbol{b}\|$ (right axis) and r/r_0 (left axis) as a function of the mass load Φ.

disperse phase increases the anisotropy of the large scales, and even more so that of the small scales. From the present analysis we can conclude that this strong effect on the small scales is due to the spectrally non-compact nature of the anisotropic back-reaction. In fact the ratio $r = \|\boldsymbol{a}\|/\|\boldsymbol{b}\|$ of small- to large-scale anisotropy (figure 17*b*) is increased up to 180 % for the largest mass load we have considered ($\Phi = 0.8$).

5. Final remarks

Clustering is a well-known feature of inertial particles advected by turbulent flows. The classical explanation of this small-scale behaviour is the centrifugal effect due to the vortical structures that populate the flow, which tend to expel heavy inertial particles from the vortex cores to localize them in the interstices between the vortices. The resulting segregation may be extremely intense for particles at Stokes numbers of order one. A peculiar feature of particle suspensions is their response to the anisotropy of the flow. In recent investigations of a particle-laden homogeneous shear flow it was found that particle clusters maintain their directionality down to the smallest scales, in ranges where the carrier velocity fluctuations already recover isotropy under the action of the Richardson cascade.

When the mass load ratio is increased, the back-reaction of the suspended phase on the carrier fluid can no longer be neglected. This opens up the issue of the role of clusters in the strong two-way coupling regime and poses the question of how the structure of the turbulence is altered by the interphase momentum exchange. This is the regime we have explored in the present paper. As main results, we find that the coupling of the carrier fluid with the suspended phase leads to less marked segregation effects, with the clusters that tend to become progressively smeared and less neatly defined with respect to the uncoupled simulation. At the same time, the anisotropy of the clusters is also reduced. Overall the trend seems to proceed towards a reduction of both the segregation and directionality of the particle configurations as the mass load Φ is increased.

The characterization of the small-scale features of the particle configurations is instrumental to understanding the modification of turbulence in the two-way coupling regime. The oriented clusters, though less defined, thickened and more isotropic than in the one-way coupling regime, constitute the geometric support of the force field

https://doi.org/10.1017/jfm.2012.503 Published online by Cambridge University Press

exerted back on the fluid. This forcing is distributed on the entire range of scales spanned by the clusters, and still present significant directionality at all active scales. In fact, we observe a selective alteration of the energy-containing scales of the fluid, as measured by a preferential modification of the three velocity variances and of the Reynolds shear stress. Overall the effects result in a sensible increase of the large-scale anisotropy of the carrier fluid measured in terms of the deviatoric component of the Reynolds stress tensor.

The observation that the back-reaction forcing occurs throughout the range of scales spanned by the clusters implies that a non-negligible amount of forcing also takes place in the smallest scales of the turbulence which, in the simplified conditions of the one-way coupling regime, are passively fed by the energy cascade from larger scales. In contrast, in the two-way coupling regime, the energy spectrum is broadened by the back-reaction, resulting in a substantial relative increase of the energy content of the smallest scales. As we have shown, the clusters, by retaining their directionality down to the smallest scales, are able to force anisotropic motions. In fact, the energy cospectrum which measures the scale-by-scale contribution to the Reynolds shear stress is found to be much less compact in spectral space than in classical shear turbulence. This leads to a substantial increase of anisotropy at the level of the instantaneous velocity gradients, as measured by the anisotropy indicator of the pseudo-dissipation tensor.

In conclusion, the structure of the system of particles and fluid is significantly altered by the coupling, an effect which increases with the amount of mass loading of the suspension. These findings could have a certain impact on turbulence modelling of multiphase flows which, both in the context of Reynolds-averaged (RANS) and filtered equations (LES), rely heavily on the concepts of inertial energy cascade and of a presumed universal statistical behaviour of the smallest scales. In fact we have shown that the cornerstone Kolmogorov theory no longer safely applies, since the classical energy cascade is overwhelmed by the anisotropy-enhancing back-reaction of the particles.

Acknowledgement

We acknowledge COST Action MP0806 for supporting mobility and CASPUR (Consorzio per le Applicazioni del Supercalcolo Per Università e Ricerca) for the provision of part of the computational resources.

REFERENCES

AHMED, A. M. & ELGHOBASHI, S. 2000 On the mechanisms of modifying the structure of turbulent homogeneous shear flows by disperse particles. *Phys. Fluids* **12** (11), 2906–2930.

BALACHANDAR, S. & EATON, J. K. 2010 Turbulent dispersed multiphase flow. *Annu. Rev. Fluid Mech.* **42**, 111–133.

BEC, J., BIFERALE, L., CENCINI, M., LANOTTE, A., MUSACCHIO, S. & TOSCHI, F. 2007 Heavy particle concentration in turbulence at dissipative and inertial scales. *Phys. Rev. Lett.* **98** (8), 084502.

BIJLARD, M. J., OLIEMANS, R. V. A., PORTELA, L. M. & OOMS, G. 2010 Direct numerical simulation analysis of local flow topology in a particle-laden turbulent channel flow. *J. Fluid Mech.* **653** (1), 35–56.

BOIVIN, M., SIMONIN, O. & SQUIRES, K. D. 1998 Direct numerical simulation of turbulence modulation by particles in isotropic turbulence. *J. Fluid Mech.* **375**, 235–263.

BOSSE, T., KLEISER, L. & MEIBURG, E. 2006 Small particles in homogeneous turbulence: settling velocity enhancement by two way coupling. *Phys. Fluids* **18**, 0271021.

https://doi.org/10.1017/jfm.2012.503 Published online by Cambridge University Press

BROOKE, J. W., KONTOMARIS, K., HANRATTY, T. J. & MCLAUGHLIN, J. B. 1992 Turbulent deposition and trapping of aerosols at a wall. *Phys. Fluids* A **6** (4), 825–834.

BURTON, T. M. & EATON, J. K. 2005 Fully resolved simulations of a particle–turbulence interaction. *J. Fluid Mech.* **545**, 67–111.

CASCIOLA, C. M. & DE ANGELIS, E. 2007 Energy transfer in turbulent polymer solutions. *J. Fluid Mech.* **581**, 419–436.

CASCIOLA, C. M., GUALTIERI, P., JACOB, B. & PIVA, R. 2005 Scaling properties in the production range of shear dominated flows. *Phys. Rev. Lett.* **95**, 024503.

CASCIOLA, C. M., GUALTIERI, P., JACOB, B. & PIVA, R. 2007 The residual anisotropy of small scales in high shear turbulence. *Phys. Fluids* **19**, 101704.

CATE, A. T., DERKSEN, J. J., PORTELA, L. M. & VAN DEN AKKEN, H. E. A. 2004 Fully resolved simulations of colliding monodisperse spheres in forced isotropic turbulence. *J. Fluid Mech.* **519**, 233–271.

CROWE, C. T., SHARMA, M. P. & STOCK, D. E. 1977 The particle-source-in-cell (PSI-CELL) model for gas-droplet flows. *J. Fluids Engng* **99**, 325–332.

DERKSEN, J. J., SUNDARESAN, S. & VAN DER AKKER, H. E. A. 2006 Simulation of mass-loading effects in gas–solid cyclone separators. *Powder Technol.* **163**, 59–68.

DRUZHININ, O. A. 1995 On the two-way interaction in two-dimensional particle-laden flows: the accumulation of particles and flow modification. *J. Fluid Mech.* **297**, 49–76.

DRUZHININ, O. A. 2001 The influence of particle inertia on the two-way coupling and modification of isotropic turbulence by microparticles. *Phys. Fluids* **13** (12), 3738–3755.

DRUZHININ, O. A. & ELGHOBASHI, S. 1999 On the decay rate of isotropic turbulence laden with microparticles. *Phys. Fluids* **11** (3), 602–610.

EATON, J. K. 2009 Two-way coupled turbulence simulations of gas-particle flows using point-particle tracking. *Intl J. Multiphase Flow* **35** (9), 792–800.

EATON, J. K. & FESSLER, J. R. 1994 Preferential concentration of particles by turbulence. *Intl J. Multiphase Flow* **20**, 169–209.

ELGOBASHI, S. 2006 An updated classification map of particle-laden turbulent flows. In *IUTAM Symposium on Computational Approaches to Multiphase Flow*, pp. 3–10. Springer.

ELGHOBASHI, S. & TRUESDELL, G. C. 1993 On the two-way interaction between homogeneous turbulence and dispersed solid particles. Part 1. Turbulence modification. *Phys. Fluids* A **5** (7), 1790–1801.

FALKOVICH, G., FOUXON, A. & STEPANOV, M. 2002 Acceleration of rain initiation by cloud turbulence. *Nature* **419**, 151.

FERRANTE, A. & ELGHOBASHI, S. 2003 On the physical mechanisms of two-way coupling in particle-laden isotropic turbulence. *Phys. Fluids* **15** (2), 315–329.

GAO, H., LI, H. & WANG, L.-P. 2011 Lattice Boltzmann simulation of turbulent flow laden with finite-size particles. *Comput. Math. Appl.* doi:10.1016/j.camwa.2011.06.028.

GARG, R., NARAYANAN, C. & SUBRAMANIAM, S. 2009 A numerical convergent Lagrangian–Eulerian simulation method for dispersed two-phase flows. *Intl J. Multiphase Flow* **35**, 376–388.

GEISS, S., DREIZLER, A., STOJANOVIC, Z., CHRIGUI, M., SADIKI, A. & JANICKA, J. 2004 Investigation of turbulence modification in a non-reactive two-phase flow. *Exp. Fluids* **36**, 344–354.

GORE, R. A. & CROWE, C. T. 1989 Effect of particle size on modulating turbulent intensity. *Intl J. Multiphase Flow* **15** (2), 279–285.

GRASSBERGER, P. & PROCACCIA, I. 1983 Characterization of strange attractors. *Phys. Rev. Lett.* **50**, 346.

GUALTIERI, P., CASCIOLA, C. M., BENZI, R. & PIVA, R. 2007 Preservation of statistical properties in large eddy simulation of shear turbulence. *J. Fluid Mech.* **592**, 471–494.

GUALTIERI, P., CASCIOLA, C. M., BENZI, R., AMATI, G. & PIVA, R. 2002 Scaling laws and intermittency in homogeneous shear flow. *Phys. Fluids* **14** (2), 583–596.

GUALTIERI, P., PICANO, F. & CASCIOLA, C. M. 2009 Anisotropic clustering of inertial particles in homogeneous shear flow. *J. Fluid Mech.* **629**, 25–39.

GUALTIERI, P., PICANO, F., SARDINA, G. & CASCIOLA, C. M. 2012 Statistics of particle pair relative velocity in the homogeneous shear flow. *Physica* D **241** (3), 245–250.

https://doi.org/10.1017/jfm.2012.503 Published online by Cambridge University Press

HETSRONI, G. 1989 Particles–turbulence interaction. *Intl J. Multiphase Flow* **15** (5), 735–746.

VAN DER HOEF, M. A., VAN SINT ANNALD, M., DEEN, N. G. & KUIPERS, J. A. M. 2008 Numerical simulations of dense gas–solid fluidized beds: a multiscale modelling strategy. *Annu. Rev. Fluid Mech.* **40**, 47–70.

HWANG, W. & EATON, J. K. 2006*a* Homogeneous and isotropic turbulence modulation by small heavy ($St \sim 50$) particles. *J. Fluid Mech.* **564**, 361–393.

HWANG, W. & EATON, J. K. 2006*b* Turbulence attenuation by small particles in the absence of gravity. *Intl J. Multiphase Flow* **32**, 1386–1396.

JACOB, B., CASCIOLA, C. M., TALAMELLI, A. & ALFREDSSON, P. H. 2008 Scaling of mixed structure functions in turbulent boundary layers. *Phys. Fluids* **20** (4), 045101.

KÁROLYI, G., PÉNTEK, A., SCHEURING, I., TÉL, T. & TOROCZKAI, Z. 2002 Chaotic flow: the physics of species coexistence. *Proc. Natl Acad. Sci.* **97**, 13661.

KOLMOGOROV, A. N. 1941 The local structure of turbulence in incompressible viscous fluid for very large Reynolds number. *Dokl. Akad. SSSR* **434**, 301–305.

KULICK, J. D., FESSLER, J. R. & EATON, J. K. 1994 Particle response and turbulence modification in fully developed channel flow. *J. Fluid Mech.* **277** (1), 109–134.

LEWIS, D. & PEDLEY, T. 2000 Planktonic contact rates in homogeneous isotropic turbulence: theoretical predictions and kinematic simulations. *J. Theor. Biol.* **205**, 377–408.

LI, Y., MCLAUGHLIN, J. B., KONTOMARIS, K. & PORTELA, L. 2001 Numerical simulation of particle-laden turbulent channel flow. *Phys. Fluids* **13** (10), 2957–2967.

LJUS, C., JOHANSSON, B. & ALMSEDT, A. E. 2002 Turbulence modification by particles in a horizontal pipe flow. *Intl J. Multiphase Flow* **28**, 1075–1090.

LOMHOLT, S. & MAXEY, M. R. 2003 Force-coupling method for particulate two phase flow: Stokes flow. *J. Comput. Phys.* **184**, 381–405.

LUCCI, F., FERRANTE, A. & ELGHOBASHI, S. 2010 Modulation of isotropic turbulence by particles of Taylor length scale size. *J. Fluid Mech.* **650** (1), 5–55.

LUCCI, F., FERRANTE, A. & ELGHOBASHI, S. 2011 Is Stokes number an appropriate indicator for turbulence modulation by particles of Taylor-length scale size? *Phys. Fluids* **23** (2), 025101.

MARCHIOLI, C. & SOLDATI, A. 2002 Mechanisms for particle transfer and segregation in a turbulent boundary layer. *J. Fluid Mech.* **468**, 283–315.

MASHAYEK, F. 1998 Droplet–turbulence interaction in low-Mach-number homogeneous shear two-phase flow. *J. Fluid Mech.* **367**, 163–203.

MAXEY, M. R. & RILEY, J. J. 1983 Equation of motion for a small rigid sphere in a non-uniform flow. *Phys. Fluids* **26**, 2437.

PAN, Y. & BANERJEE, S. 2001 Numerical simulation of particle interaction with wall turbulence. *Phys. Fluids* **8** (10), 2733–2755.

PARIS, A. D. & EATON, J. K. 2001 Turbulence attenuation in particle-laden channel flow. Stanford PhD thesis of Paris, A.D., TSD-137, Department of Mechanical Engineering.

PICANO, F., SARDINA, G. & CASCIOLA, C. M. 2009 Spatial development of particle-laden turbulent pipe flow. *Phys. Fluids* **21**, 093305.

POELMA, C. & OOMS, G. 2006 Particle–turbulence interaction in homogeneous isotropic turbulent suspension. *Appl. Mech. Rev.* **50**, 78–90.

POELMA, C., WESTERWEEL, J. & OOMS, G. 2007 Particle–fluid interaction in grid-generated turbulence. *J. Fluid Mech.* **589**, 315–351.

POESIO, P., OOMS, G., CATE, A. T. & HUNT, J. C. R. 2006 Interaction and collisions between particles in a linear shear flow near a wall at low Reynolds number. *J. Fluid Mech.* **555**, 113–130.

POPE, S. B. 2000 *Turbulent Flows*. Cambridge University Press.

PORTELA, L. M., COTA, P. & OLIEMANS, R. V. A. 2002 Numerical study of the near-wall behaviour of particles in turbulent pipe flow. *Powder Technol.* **125**, 149–157.

POST, S. L. & ABRAHAM, J. 2002 Modelling the outcome of drop–drop collisions in diesel sprays. *Intl J. Multiphase Flows* **28** (6), 997–1019.

PUMIR, A. 1996 Turbulence in homogeneous shear flow. *Phys. Fluids* **8** (11), 3112–3127.

PUMIR, A. & SHRAIMAN, B. 1994 Persistent small scale anisotropy in homogeneous shear flow. *Phys. Rev. Lett.* **75** (11), 3114–3117.

https://doi.org/10.1017/jfm.2012.503 Published online by Cambridge University Press

RANI, S. L., WINKLER, C. M. & VANKA, S. P. 2004 Numerical simulations of turbulence modulation by dense particles in a fully developed pipe flow. *Powder Technol.* **141**, 80–99.

READE, W. C. & COLLINS, L. R. 2000 Effect of preferential concentration on turbulent collision rates. *Phys. Fluids* **12**, 2530.

REEKS, M. W. 1983 The transport of discrete particles in inhomogeneous turbulence. *J. Aerosol Sci.* **14** (6), 729–739.

ROGALLO, R. S. 1981 Numerical experiments in homogeneous turbulence. NASA Technical Memorandum 81315.

ROUSON, D. W. & EATON, J. K. 2001 On the preferential concentration of solid particles in turbulent channel flow. *J. Fluid Mech.* **428**, 149.

SADDOUGHI, S. G. & VEERAVALLI, S. V. 1994 Local isotropy in turbulent boundary layers at high Reynolds number. *J. Fluid Mech.* **268** (333–372).

SHOTORBAN, B. & BALACHANDAR, S. 2006 Particle concentration in homogeneous shear turbulence simulated via Lagrangian and equilibrium Eulerian approaches. *Phys. Fluids* **18**, 065105.

SHUMACHER, J. 2004 Relation between shear parameter and Reynolds number in statistically stationary turbulent shear flows. *Phys. Fluids* **16** (8), 3094–3102.

SOLDATI, A. & MARCHIOLI, C. 2009 Physics and modelling of turbulent particle deposition and entrainment: review of a systematic study. *Intl J. Multiphase Flow* **35** (9), 827–839.

SQUIRES, K. D. & EATON, J. K. 1990 Particle response and turbulence modification in isotropic turbulence. *Phys. Fluids* A **2** (7), 1191–1203.

STRESING, R., PEINKE, J., SEOUD, R. E. & VASSILICOS, J. C. 2010 Defining a new class of turbulent flows. *Phys. Rev. Lett.* **104** (19), 194501.

SUNDARAM, S. & COLLINS, L. 1996 Numerical considerations in simulating a turbulent suspension of finite-volume particles. *J. Comput. Phys.* **124**, 337–350.

SUNDARAM, S. & COLLINS, L. R. 1997 Collision statistics in an isotropic particle-laden turbulent suspension. Part 1. Direct numerical simulations. *J. Fluid Mech.* **335**, 75–109.

SUNDARAM, S. & COLLINS, L. R. 1999 A numerical study of the modulation of isotropic turbulence by suspended particles. *J. Fluid Mech.* **379**, 105–143.

TANAKA, T. & EATON, J. K. 2008 Classification of turbulence modulation by disperse spheres using a novel dimensionless number. *Phys. Rev. Lett.* **101**, 114502.

TANAKA, T. & EATON, J. K. 2010 Sub-Kolmogorov resolution particle image velocimetry measurements of particle-laden forced turbulence. *J. Fluid Mech.* **643**, 177–206.

WANG, L. P., AYALA, O., ROSA, B. & GRABOWSKI, W. W. 2008 Turbulent collision efficiency of heavy particles relevant to cloud droplets. *New J. Phys.* **10**, 1–40.

WANG, L. P., ROSA, B., GAO, H., HE, G. & JIN, G. 2009 Turbulent collision of inertial particles: point-particle based, hybrid simulations and beyond. *Intl J. Multiphase Flow* **35** (9), 854–867.

WOODS, W. A. 2010 Turbulent plumes in nature. *Annu. Rev. Fluid Mech.* **42**, 391–412.

YANG, T. S. & SHY, S. S. 2005 Two-way interaction between solid particles and homogeneous air turbulence: particle settling rate and turbulence modulation measurements. *J. Fluid Mech.* **526**, 171–216.

YEO, K., DONG, S., CLIMENT, E. & MAXEY, M. R. 2010 Modulation of homogeneous turbulence seeded with finite size bubbles or particles. *Intl J. Multiphase Flow* **36** (3), 221–233.

YOSHIMOTO, H. & GOTO, S. 2007 Self-similar clustering of inertial particles in homogeneous turbulence. *J. Fluid Mech.* **577**, 275–286.

ZHANG, Z. & PROSPERETTI, A. 2005 A second-order method for three-dimensional particle simulation. *J. Comput. Phys.* **210**, 292–324.

ZHAO, L. H., ANDERSSON, H. I. & GILLISEN, J. J. 2010 Turbulence modulation and drag reduction by spherical particles. *Phys. Fluids* **22**, 0817021.

https://doi.org/10.1017/jfm.2012.503 Published online by Cambridge University Press